Scintillating fibre detector and kinematic fitting for the BGO-OD experiment

Masterarbeit in Physik

von
Stefan Alef

angefertigt im
Physikalischen Institut,
Rheinische Friedrich-Wilhelms Universität Bonn

vorgelegt der
Mathematisch-Naturwissenschaftlichen Fakultät der Universität Bonn

September 2015

1. Gutachter: Prof. Dr. Hartmut Schmieden
2. Gutachter: Prof. Dr. Philip Cole

Contents

1. Introduction

In 1961 Murray Gell-Mann provided the world of particle physics with an unique ordering scheme for light mesons and baryons [1]. In this *Eightfold Way* the hadrons are composed of either two or three constituent quarks. This breakthrough allowed physicists for the first time to understand the nature of the vast *particle zoo* of hadrons that had been discovered.

Experiments, e.g. deep-inelastic electron-proton scattering confirmed the existence of quarks and gluons [26], but also revealed that the static picture proposed by Gell-Mann is not sufficient to describe the inner dynamics of the hadron. A crucial aspect that needs to be further understood, is the hadron excitation spectrum. Of particular interest is the excitation of baryons, in which the excited state decays into a meson-baryon system. Experimentally this can be studied by meson photoproduction, for which several experiments worldwide have been developed, one of those being the BGO-OD experiment.
There are indications for meson-baryon interaction in the formation of those excited states [36]. Due to the weakness of the residual strong force between the hadrons, these states are only loosely bound and have to be observed under special kinematic conditions. The layout of the BGO-OD experiment was specifically designed to match those conditions.

To understand the physical processes in the experiment a sufficient resolution is essential. One way to improve the energy resolution of the whole experiment, is to optimize the resolution of the initial photon beam energy. To do so the existing BGO-OD detector system was complemented with a scintillating fibre detector. This thesis describes the development and set-up of said detector. It was named ARGUS after the all-seeing one-hundred-eyed giant from Greek mythology.

With ARGUS the resolution of the initial photon energy will be improved. It is however still possible to improve the resolution and maximise the potential of all detectors in the experiment by applying the analysis technique of kinematic fitting to the already taken data. A mathematical procedure for kinematic fitting was written by Paul Avery [2] and its main idea is to vary the parameters obtained in the experiment (e.g. energies and directions of the particles) within their errors to fulfil a set of given constraints, e.g momentum conservation or the invariant mass in particle decays.
Together with ARGUS this will make it possible to detect reactions that are difficult to observe otherwise, e.g. $\gamma p \to K^0\Sigma^+$.

The first part of this thesis will explain the theoretical background that lead to the

development of the experiment in more detail, in particular reasons why the naive quark model is not sufficient, while the second chapter will explain the BGO-OD experiment. This will be followed by a description of the development of ARGUS, which was done in cooperation with Björn-Eric Reitz [3]. The last part of this thesis concerns itself with the set-up of a kinematic fit to the already observed reaction $\gamma p \to \pi^0 p$, which will work as a test for the kinematic fitting.

2. Theoretical background

After Gell-Mann's formulation of the Eightfold Way, the electroweak unification formulated by Sheldon Glashow, Stephen Weinberg and Abdus Salam [4, 5, 6] and the confirmation, that hadrons are actually made up of quarks, ultimately led to the development of the *Standard Model of particle physics* in the 1970's. This chapter explains the basics of the Standard Model with a special emphasis on hadrons, which are the objects investigated by the BGO-OD experiment.

2.1. The Standard Model

The Standard Model of particle physics describes all known elementary particles and all fundamental forces, except gravity. In the context of the Standard Model all fundamental forces are mediated via exchange particles, the gauge bosons, making it possible to describe most known processes solely through particle interactions.
The strong force couples only to particles carrying a colour, which can be viewed as the charge of the strong force. There are three colours and their respective anti-colours: red, green and blue. The strong force is mediated by eight massless gluons each carrying colour and anti-colour. The coupling $\alpha_s \approx 1$ of the strong force is not constant with respect to energy and distance, which can be seen in figure 2.1. As a result the strong force increases with distance. Nonetheless, of the four fundamental forces, the strong force has the biggest coupling constant.

The electromagnetic force is mediated by the massless photon, it couples only to particles that carry an electric charge. The coupling constant of the electromagnetic force is the fine structure constant $\alpha \approx 1/137$, which is two orders of magnitude smaller than the coupling constant of the strong force.
The weak force is carried by the massive $W^{\pm}$-bosons and the also-massive Z-boson. It's coupling constant $\alpha_w \approx 10^{-6}$ is the smallest of the three interactions described by the Standard Model.
All massive elementary particles are given their mass via the Higgs mechanism. The Higgs boson is the gauge boson of the Higgs mechanism and a massive particle itself. It is the only gauge boson with a spin of zero.

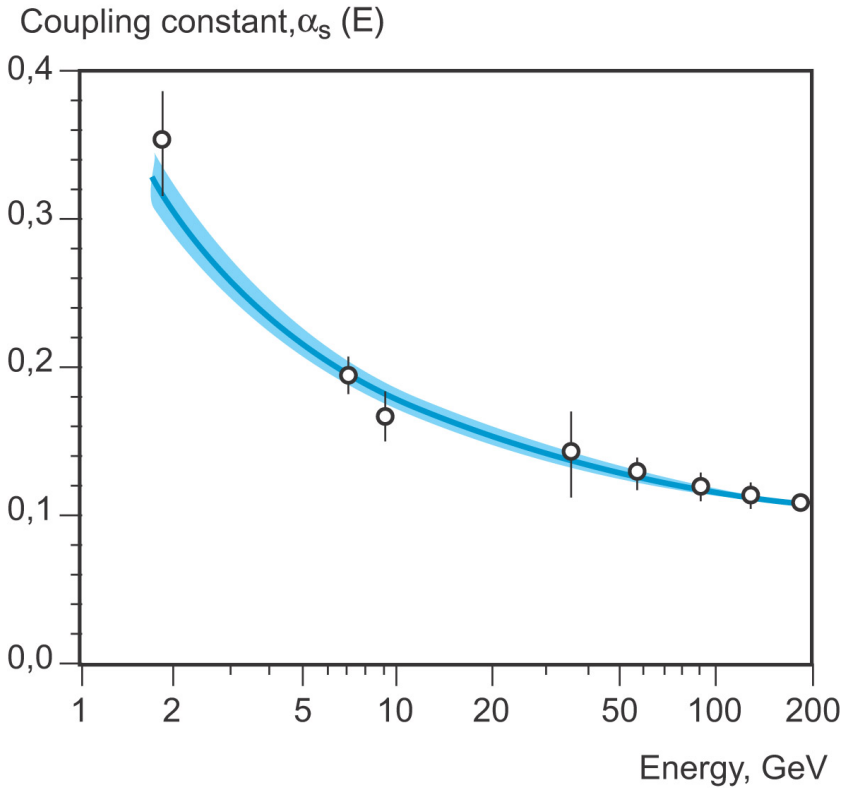

Figure 2.1.: Energy dependence of the strong coupling constant α_s [7].

Apart from the previously described gauge bosons, there are two other groups of particles in the Standard Model, the leptons and the quarks. Baryonic matter, the matter we observe around us is composed out of those particles.
Leptons are Spin-1/2 fermions that can appear either charged or uncharged. The leptons can be grouped in three generations, each consisting of a charged and an uncharged lepton. Leptons all interact via the weak force, in the case of the charged leptons also via the electromagnetic interaction. The uncharged leptons, the neutrinos, are near massless (see figure 2.2).
Quarks are the third group of particles in the Standard Model, they are also Spin-1/2 fermions and carry fractional charges of +2/3 or -1/3. Like the leptons, quarks can be grouped in three generations with each generation consisting of a positively and negatively charged quark and each generation being heavier than the previous. Due to the fact, that in addition to their charge quarks also carry a colour, they are subject to the strong force. A deeper look into the subject of quarks can be found in the next chapter. Figure 2.2 shows all particles of the Standard Model, as well as their respective interactions.

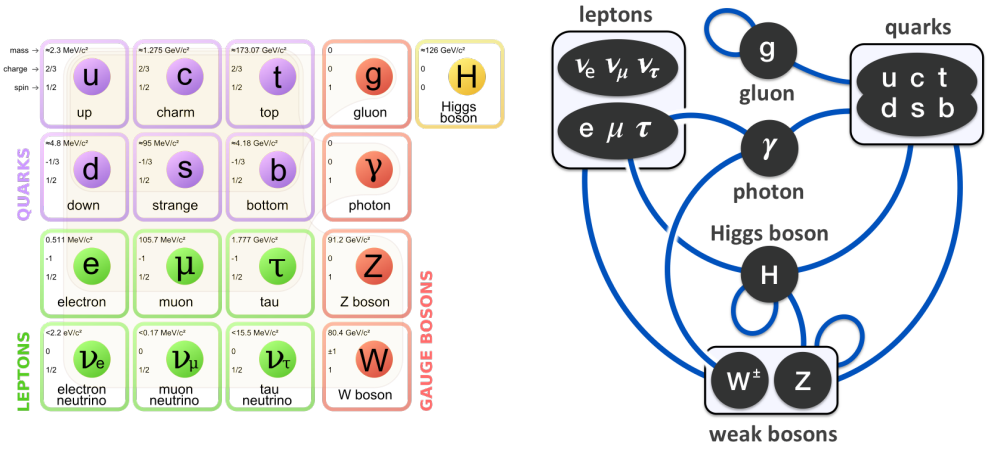

Figure 2.2.: Overview of the particles of the Standard Model (left) and their interactions with each other (right). The blue lines indicate, that these particles can interact with each other via one of the fundamental forces. As can be seen from the figure some particles are able to interact with themself, e.g. the Higgs boson [8].

2.2. Hadrons and the strong force

As mentioned above quarks are subject to the strong force. The strong force is described by Quantum-Chromo-Dynamics (QCD). Since the strong force is stronger than the electromagnetic force by two orders of magnitude, quarks are bound by the strong force. They can never appear as free particles and are only seen in colourless bound states, this is called confinement. Confinement is a result of the fact, that the strong force increases with range, which is in contrast to the other forces, that decrease with range. A colourless state is either achieved by combining a colour with its anti-colour (e.g. red and anti red) or by combining all three colours (red, green and blue).
The simplest way to form a colourless object is to combine a quark with an anti quark ($q\bar{q}$), the resulting particle is called a meson. This is a simplified picture, nevertheless this easy model allowed Gell-Mann to develop an effective ordering scheme for mesons consisting of light quarks (u,d,s). Since both quarks carry spin 1/2 there are two possible ways to order these spins, parallel and anti-parallel.
For anti-parallel spins the resulting total angular momentum (assuming the angular momentum between the two constituents is zero) and parity are $J^P = 0^-$, these mesons are called pseudo scalar. Group theory dictates, that the 3×3 possible combinations of quarks will then yield an octet and a singlet [35]. Those are the states, which are physically observed, except for the η, η' and π^0, which are mixtures of different octet and singlet states. All physical states can be seen in figure 2.3 on the right.
Similar to this case a scheme for mesons with parallel spin and therefore $J^P = 1^-$ can be developed; these are called vector mesons. The resulting octet and singlet again partly mix to form the observed particles seen in figure 2.3 on the left.

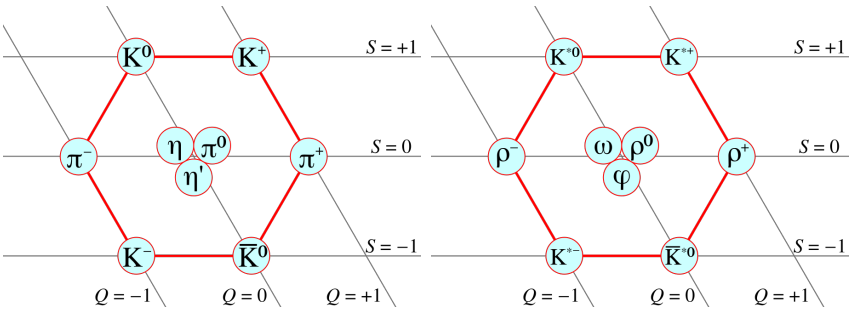

Figure 2.3.: Pseudo scalar (left) and vector mesons (right) [9]. The η, η' and π^0 as well as the ρ^0 and ω are mixtures of octet and singlet states, whereas the ϕ is a pure $s\bar{s}$ state. The other particles are no mixtures of different states.

Another way of forming a colourless object from quarks is combining three quarks (qqq). These particles are called baryons. Similar to the mesons, there are two ways of combining the three spins of the quarks. Either all spins are parallel, resulting in a $J^P = 3/2^+$ configuration or only two of the spins are parallel, creating a $J^P = 1/2^+$ particle. For $J^P = 3/2^+$ this results in ten possible combinations of three quarks, the baryon decuplet (see figure 2.4 on the left). For $J^P = 1/2^+$ the combinations uuu, ddd and sss are not possible due to symmetry reasons, resulting in a baryon octet, see figure 2.4 on the right. In contrast to the meson sector there is no mixing between different baryonic states.

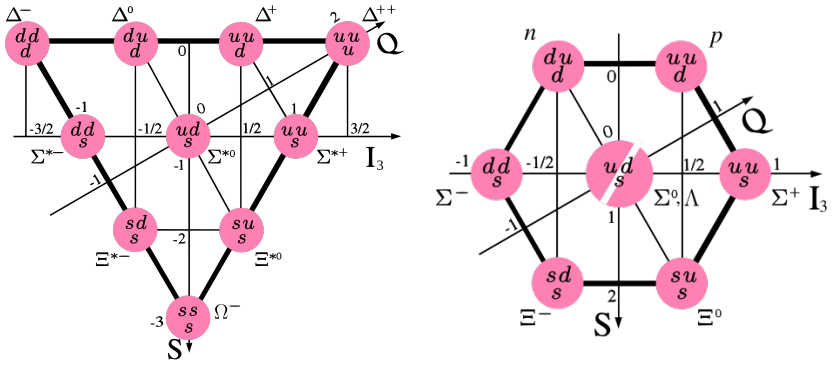

Figure 2.4.: Baryon decuplet (left) and baryon octet (right) [10].

In general QCD also allows bound states of $qq\overline{qq}$ and $qqqq\bar{q}$ (*pentaquarks*). This could also be seen as two bound mesons and a bound system of baryon and meson, respectively. A possible pentaquark state has recently been observed at LHCb at CERN [29]. Also candidates for tetra quarks have been discovered (e.g. the X(3872) [32]).

This picture, although it is convenient for ordering the particles, is too naive for a complete description, since it does not include the internal dynamics of the baryon. This becomes evident, when looking at some basic properties of the nucleon. Just adding the masses of the three current quarks of the nucleon yields an expected mass of

$\approx 10\,\mathrm{MeV}$ which is of course far from the well known nucleon mass of 939 MeV [11]. Also experiments have shown, that the spins of the three constituents only account for approximately 30% [30] of the total spin. The experimental parity ordering of the nucleon excitation spectrum also does not agree with theory. Within quark potential models, that view the hadron as a potential well created by the quarks, in which the quarks reside, the next heavier excitation after the ground state nucleon should have inverse parity (therefore parity $-$). So far no experimental evidence of such a state has been found, see figure 2.5.

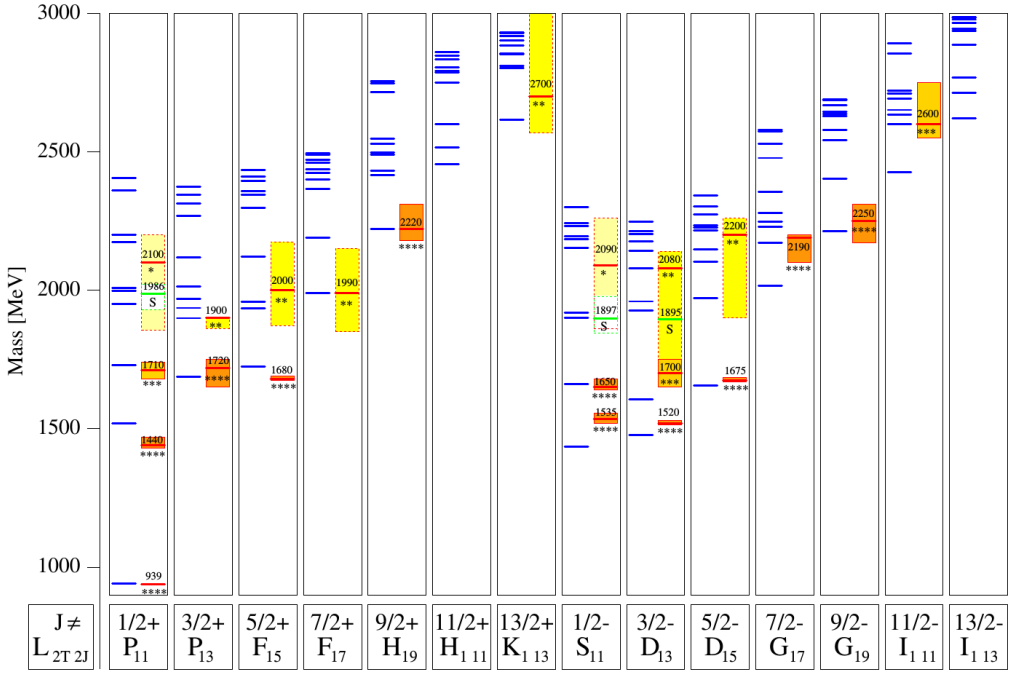

Figure 2.5.: Excitation spectrum of the nucleon in the quark potential model [12]. Blue are the theoretically predicted, while red are the experimentally found resonances. The boxes around the found resonances indicate the error on their mass.

To explain these discrepancies more evolved models can be used. In those the field energy of the strong interaction between the constituent quarks leads to a gluon field inside of the hadron that produces short-lived light quark-anti-quark pairs (sea quarks) within Heisenberg's uncertainty relation. Hence the hadron is no longer a static object but a dynamic system of quarks and gluons. In this context the mass of the hadron almost exclusively stems from the energy of the strong field.
Taking this idea a step further, not only sea quarks, but also colour-neutral states, light mesons like pions, can be produced from the field. The hadron is then a composed object. One example for such a model is the *Cloudy Bag* [33] model in which a baryon is seen as an inner three quark core surrounded by a cloud of pions. These mesons then also contribute to the mass and the total spin of the hadron.
Exciting a baryon with enough energy would accordingly lead to the creation of another

meson. This is energetically more favoured than simple sea quarks, since the meson is colourless. The system of baryon and produced meson is only lightly bound by the residual strong force between the two objects. In the example of the Cloudy Bag model, the excitation of the pion cloud also affects the total parity of the excited system and is therefore a possible solution for the problem of the parity ordering, see again figure 2.5.

In order to produce such a system in an experiment it is necessary to keep the momentum transferred onto the system below the binding energy to not destroy it. Hence, other particles involved in the production must take over the momentum. In the case of a fixed target experiment, said particle consequently has a high momentum in forward direction. Due to the therefore low momentum, the system itself will decay almost at rest and hence isotropically around the target. For this reason an experimental set-up for the detection of excited meson/baryon decays needs to be able to detect the forward going particle and the centrally decaying excited states.

To validate and further investigate the new dynamic hadronic models a series of new experiments have been developed (CBELSA [13], CLAS [14], LEPS [15]), one of those being the BGO-OD experiment [16].

3. The BGO-OD experiment

The BGO-OD experiment located at the Elektronen-Stretcher-Anlage (ELSA) at the University of Bonn is a fixed target experiment in which mesons are produced via photoproduction. Due to the particular event topology of excited meson decays the set-up of the experiment was chosen such that it ideally fits the experimental constraints explained in the chapter before.
In this chapter the basic set-up of the experiment and its working principle are explained. Some components, which are also relevant for the construction of ARGUS, are explained in more detail. The chapter also includes a mathematical explanation to the kinematic fitting.

3.1. The ELSA accelerator

ELSA is a three stage electron accelerator delivering final energies of up to 3.5 GeV. Figure 3.1 shows the complete accelerator.

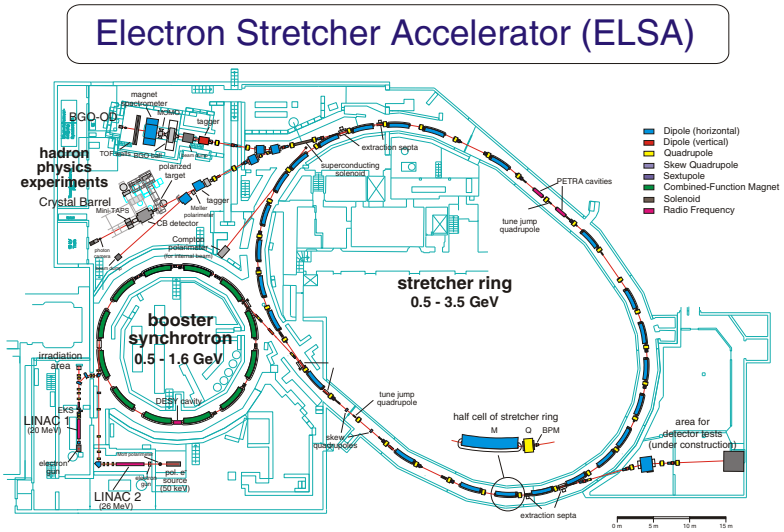

Figure 3.1.: Overview of the ELSA accelerator [17].

Electrons can be produced either polarised or unpolarised and are then accelerated by one of two linear accelerators. Subsequently they are fed into a booster synchrotron from

where they are injected in the final stretcher ring. The electron beam can be extracted into the areas of the two hadron physics experiments, BGO-OD and CB (Crystal Barrel). There is also an area for tests with synchrotron radiation.

3.2. The BGO-OD experiment

The BGO-OD (**BGO**-calorimeter **O**pen-**D**ipole forward spectrometer) experiment was initialized in 2010, supported by the DFG. The experiment posts a unique set-up, consisting of a $0.9 \cdot 4\pi$ central Bismuth germanium oxide (BGO, $Bi_4Ge_3O_{12}$) calorimeter and a forward spectrometer. With this design BGO-OD is ideally suited for the detection of excited meson decays as explained in 2.2. Figure 3.2 shows an overview of the complete set-up.

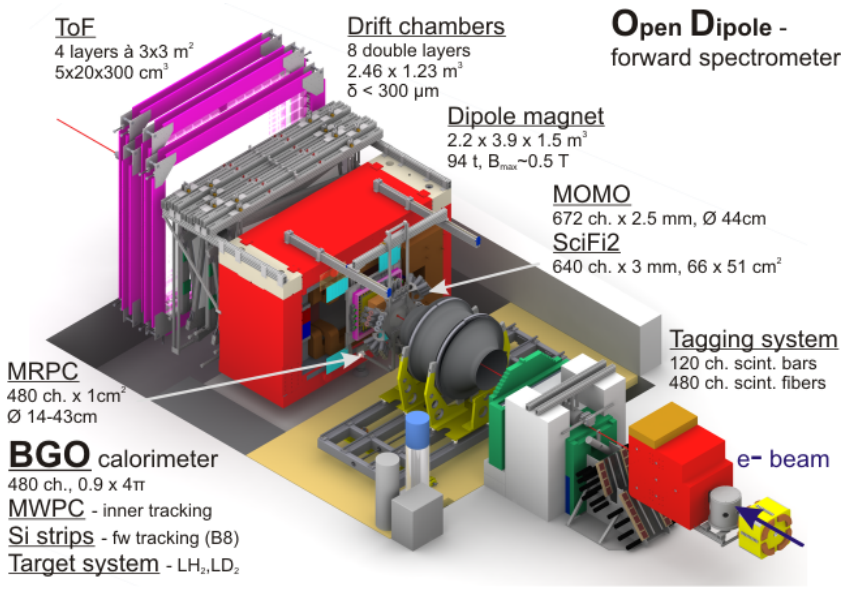

Figure 3.2.: Overview of the complete BGO-OD setup. The picture still shows the old tagger, for the current tagger see figure 3.3 [16].

A beam of real photons, which can have different polarisations (see 3.4), is produced through bremsstrahlung (see 3.3) in a radiator placed in a goniometer. The goniometer allows the use of different radiators (50 μm Cu, 100 μm Cu, 200 μm Cu, diamond) in the electron beam, as well as to rotate the diamond radiator.
The trajectories of the post-bremsstrahlung electrons are bent into the tagging system by a dipole magnet. The tagging system consists of 120 scintillator bars and can be divided into a horizontal and a vertical part. The horizontal part lies in the focal plane of the tagging magnet. Because space is limited by the beam dump in which electrons that did not undergo bremsstrahlung are bend, the second part of the tagger has to go in vertical direction. The trajectories of electrons of different energy are curved by different

amounts by the tagging magnetic field, therefore allowing the tagging system to calculate an electron's energy, by measuring its position. Combined with the information of the initial ELSA energy, this allows for the calculation of the produced photon's energy, see figure 3.3 on the right side. The energy resolution of the tagging system is $(0.5-2.1)\% \cdot E_0$ over a range of $(10-90)\% \cdot E_0$.
Figure 3.3 shows an overview of the tagging system, the ARGUS detector will be located in front of the current set-up.

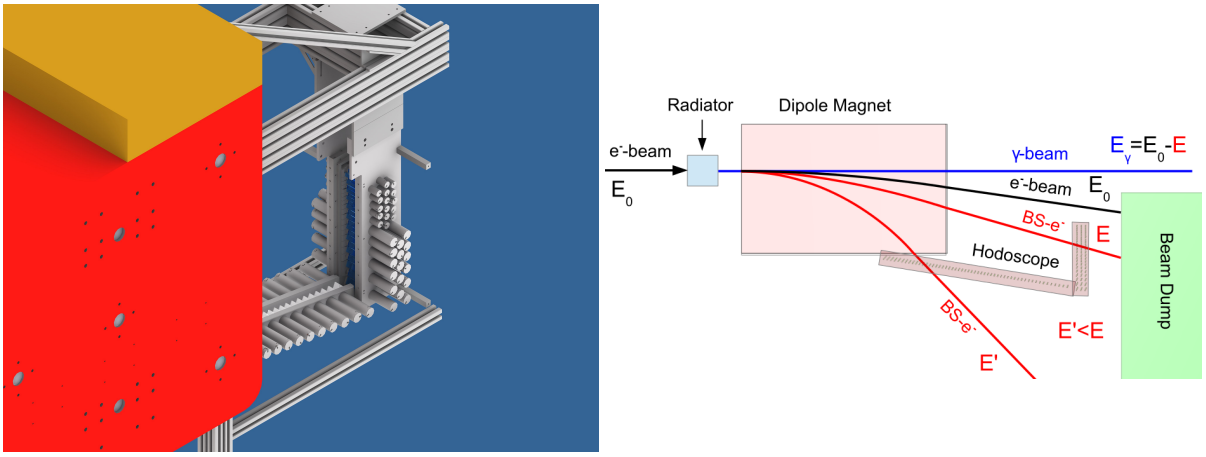

Figure 3.3.: Current BGO-OD tagger set-up (left) and its mode of operation (right) [18]. Electrons of different energy are bend with different radii in the tagger magnet. Hence measuring the position of the electron after it underwent bremsstrahlung makes it possible to calculate its energy.

The produced photons are collimated and enter the target, which can be filled with either liquid hydrogen or liquid deuterium or alternatively a solid target (e.g. carbon). The target itself is surrounded by a silicon strip barrel and two Multiwire-Proportional-Chambers, which enable tracking of charged particles close to the target and particle identification via dE/dx measurement in the barrel.
Surrounding this setup is the central calorimeter, the BGO ball. Consisting of 480 crystals and covering a solid angle of $0.9 \cdot 4\pi$, it is well suited for photon detection and also for proton detection up to a kinetic energy of 450 MeV. Particles are detected by producing an electromagnetic shower inside the BGO crystals. If the shower produces signals in adjacent crystals, a cluster can be formed. The position of this cluster yields a ϕ and a θ angle for the detected particle. Its kinetic energy is calculated from the energy deposited in the BGO ball.

The central part of the experiment is followed by the forward spectrometer. Embedded into the back part of the BGO ball is the Scintillating ring detector, used for the tracking of forward going protons. It is followed by a Multi-resistive-plate-chamber and two silicon tracking detectors (Momo, SciFi2). The spectrometer is completed by the open dipole magnet on permanent lease from the GSI Darmstadt, a set of 8 drift

chambers and 4 time-of-flight walls, used for particle identification.

The photon flux monitor is located at the end of the experiment, designed to measure the total photon flux, and thereby deliver a normalisation for cross section measurements.

3.3. Bremsstrahlung

The photon beam for the BGO-OD experiment is produced via bremsstrahlung in one of the radiators in the goniometer. Bremsstrahlung occurs, when a charged particle moves through an electric field. The resulting acceleration forces the particle to emit a photon. Due to momentum conservation a recoil partner is needed for the process, i.e. if an electron undergoes bremsstrahlung in the field of a nucleus, said nucleus will take over a small but non-negligible recoil momentum. Bremsstrahlung is proportional to $1/m^2$, m being the mass of the particle. It is therefore highly suppressed for heavier particles and is mostly a phenomenon occurring for electrons. Figure 3.4 shows Feynman graphs of the process.

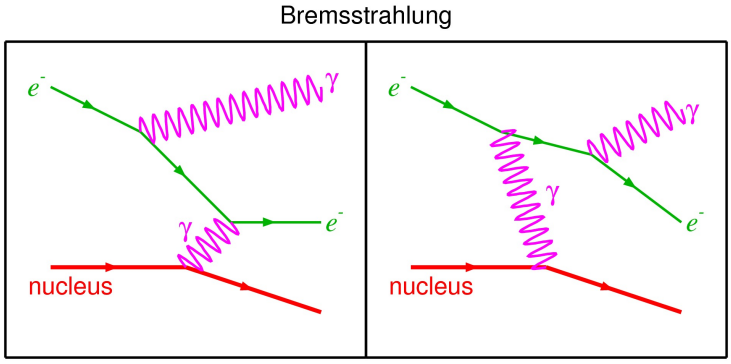

Figure 3.4.: Feynman graphs for the process of bremsstrahlung [21]. In both cases the nucleon is needed to take over the recoil.

Since the energy of the initially incoming particle is shared between two final state particles, the energy spectrum for each of those is continuous. The photon energy spectrum has a $1/E$ structure, E being the photon energy, and is therefore peaked towards lower energies of the radiated photon, see figure 3.5.

If bremsstrahlung occurs in a crystalline structure, like a diamond, it is possible, that the recoil momentum is not taken over by a single atom, but by the whole crystal. For that it is necessary, that the recoil momentum vector lies in the same plane as and matches the reciprocal lattice vector. Since the recoil is taken by not one, but many atoms, the probability of bremsstrahlung is greatly enhanced, leading to a peak in the bremsstrahlung spectrum for an energy where the conditions for the recoil momentum

are fulfilled. Of course in reality not one, but several lattice vectors will contribute, creating several peaks at different photon energies. A bremsstrahlung spectrum with coherent contribution can be seen in figure 3.5. The enhancement becomes even clearer, if the spectra are divided.

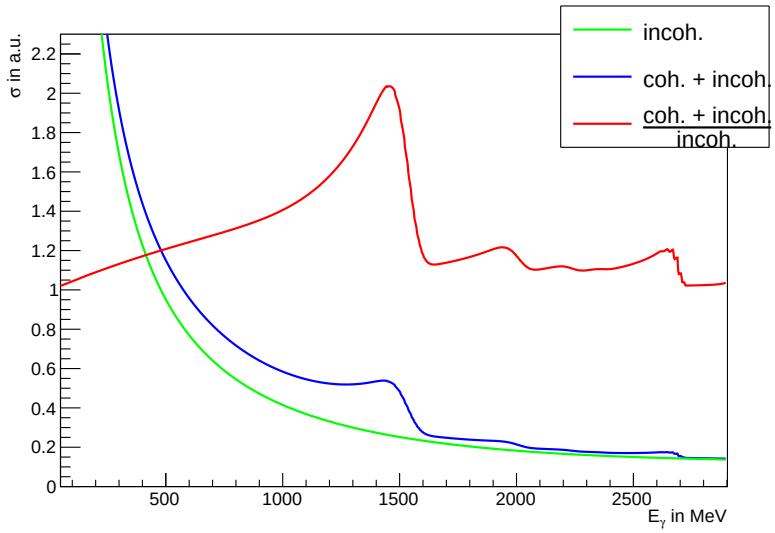

Figure 3.5.: Spectrum for incoherent bremsstrahlung from an amorphous radiator (green), incoherent bremsstrahlung with coherent component obtained from a diamond radiator (blue) and the latter one normalised to the incoherent spectrum (red) [20].

3.4. Polarisation at BGO-OD

Since ELSA is able to deliver polarised electrons, at BGO-OD also a polarised photon beam can be produced trough bremsstrahlung.
Photons can be described by an electromagnetic wave. If the electric part of that wave oscillates in a certain plane, the photon is called linearly polarised. If two of those linear polarisations overlap with a certain phase the resulting polarisation is called elliptic, since the electric field vector moves on an ellipsis. In the special case of a 90 ° phase the polarisation is called circular. Figure 3.6 shows the different types of polarisations.

At BGO-OD linear polarisation of the produced photon beam can be achieved by shooting the unpolarised ELSA electron beam onto a thin diamond radiator. Since the crystal planes of the diamond force a certain plane for the coherent bremsstrahlung recoil (see chapter 3.3), the electric field vector also lies in said plane, resulting in a linear polarisation of the those photons, which underwent coherent bremsstrahlung.
For circular polarisation, the longitudinally polarised ELSA electron beam is shot onto a copper radiator. The electron spin will hereby point in or opposite to the momentum direction, thus the electron has positive or negative helicity. Due to helicity conservation,

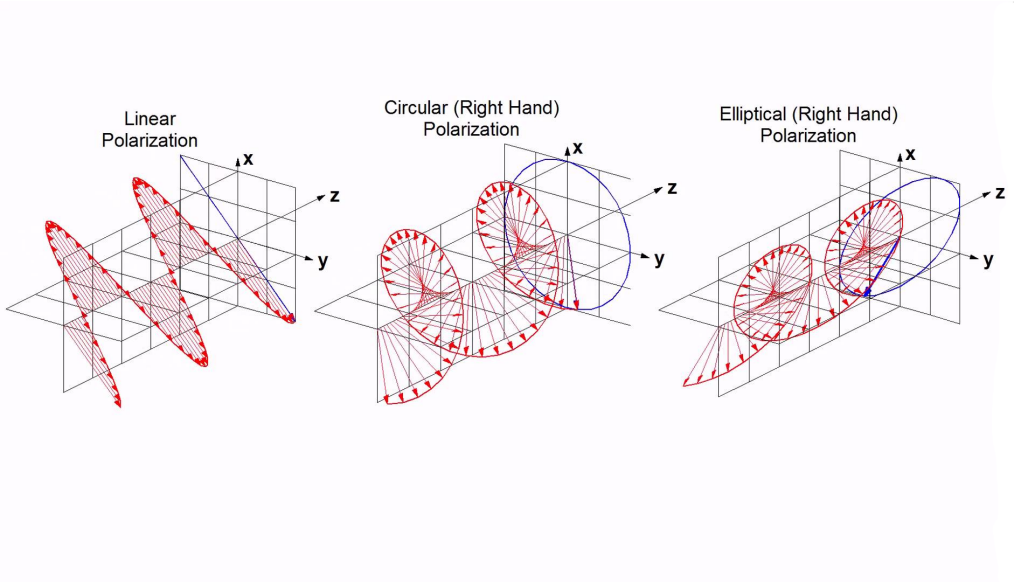

Figure 3.6.: Different types of polarisations. Elliptical and circular polarisation can rotate in either direction depending on the sign of the phase, which is called left- or right-handed [19].

the helicity must be partly or as a whole transferred to the produced photon, creating a circular polarisation for the photon. How much of the helicity is transferred to the photon depends on the amount of energy the photon takes in the process of bremsstrahlung, see figure 3.7.

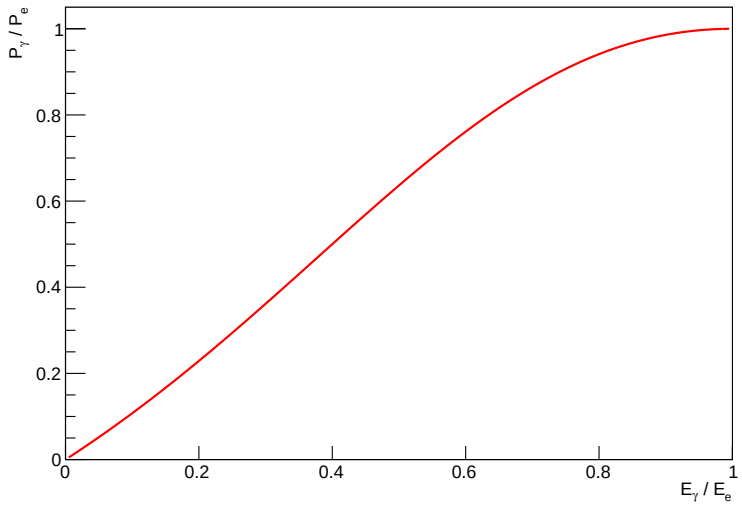

Figure 3.7.: Energy dependence of the helicity transfer in the process of bremsstrahlung [20].

3.5. Scintillation

For a measurement in particle physics it is necessary to know the four-momentum and particle type of the particles in the final state. To measure the direction of the four-momentum, detectors are used that measure the position of a particle without stopping it in the process.
Scintillation is a reaction suited for such detectors. It is used in some of the detectors of BGO-OD (the tagger, the barrel inside the BGO ball, SciFi2, MOMO and the ToF walls) and is also used for ARGUS.
Scintillation is a mechanism of creating light in a transparent material when a particle passes through. The incoming particle excites a valence electron in the material to a higher energetic level. Said electron will de-excite after some time. Some of these de-excitations take place internally and are not visible. Others produce fluorescence or phosphorescence. The produced photons can then be detected via a photomultiplier. Figure 3.8 shows the working principle.

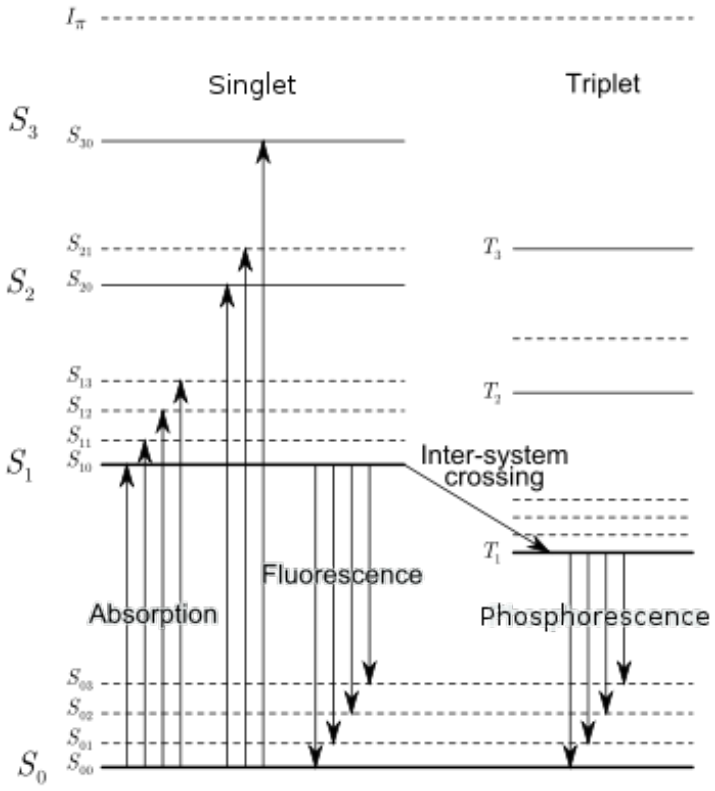

Figure 3.8.: Principle of scintillation: a valence electron is excited by a passing particle. The fluorescence or phosphorescence that occur when the excited electron de-excites can be detected via a photomultiplier [22].

3.6. Photomultipliers

Photomultipliers (PMT) are an instrument to detect photons, figure 3.9 shows the schematics of a typical PMT. PMTs are used to detect the scintillator photons in ARGUS.
Incoming photons (e.g. produced by a scintillator) hit a photo cathode, where they produce an electron. The probability to do so is called quantum efficiency. This electron is subsequently guided on a set of dynodes. On the first dynode the produced electron will free additional electrons. Those are then pulled to the next dynode by the internal electric fields. On each dynode the electrons will free additional electrons from the dynode, thus increasing the number of electrons that hit the following dynode. Hence at the end it is not a single electron, but an avalanche that hits the anode, thereby creating a strong signal that can easily be detected and read out by electronics like a Time-over-threshold discriminator. Typical values for this enhancement, also called gain, are 10^7.

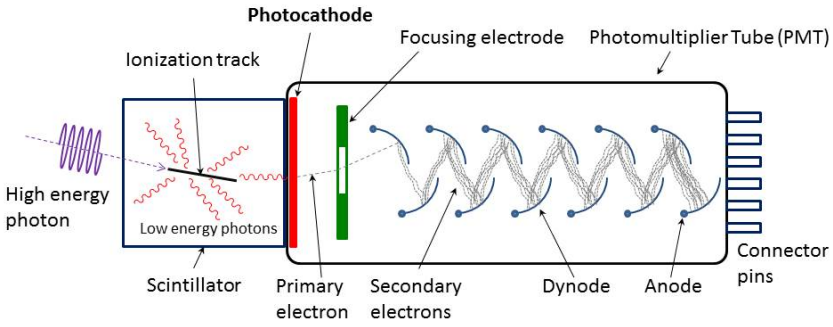

Figure 3.9.: Schematics of a photomultiplier with attached scintillator [23].

3.7. Time-over-threshold discriminators

Time-over-threshold (ToT) is a way to measure an analogue signals magnitude by comparing it to a previously set threshold and to convert the analogue to a digital signal. Figure 3.10 shows the basic principles of ToT. ToT discriminators are used to detect the analogue signals from the PMTs inside ARGUS.

If the analogue signal surpasses the threshold the digital signal will start. It will be stopped when the analogue signal falls below the threshold again. Therefore the length of the digital signal corresponds to the height and the length of the analogue signal, i.e. its magnitude.
Sometimes the analogue signal is not smooth, but has a sub structure, e.g. secondary peaks. As can be seen in figure 3.10 this can occasionally result in the signal dipping below the threshold and thereby creating a second signal. Of course this could be avoided by setting a lower threshold, though in some cases this is not desirable (e.g. if too much noise is picked up by lowering the threshold). Another way of avoiding this problem, is to use an hysteresis.

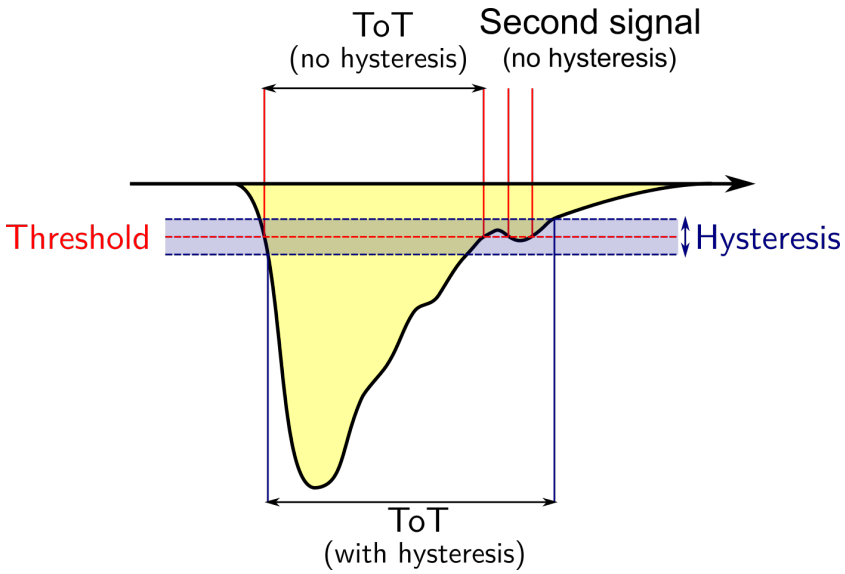

Figure 3.10.: Working principle of the time-over-threshold method with and without hysteresis [31].

The hysteresis sets a band around the originally chosen threshold. The digital signal now starts when the analogue signal surpasses the upper end of the band and it ends when it falls below the lower end. That way some substructures are still counted towards the original analogue signal.

3.8. The explora framework

After the experiment has been performed the data taken must be further analysed to extract the physical processes that took place in the target. At BGO-OD the explora framework is used for the analysis of data as well as for simulations.
Explora is a xml-based framework where users can write plug-ins in C++/Root for different parts of an analysis, e.g. particle four-momentum reconstruction. These plug-ins will then be called in the final xml-files making it easy to extend an explora analysis by additional modules. The simulations are not done by explora itself, but by GEANT4 [27] and VMC Virtual Monta Carlo [28], which explora can access.
Explora allows several people to work on the same plug-in and then merge the different versions. It was originally developed for the CB experiment, but a lot of new plug-ins have been written for BGO-OD.
All the analysis and simulation performed in this work, was done in explora.

3.9. Kinematic Fitting

Kinematic fitting is a software technique to improve the resolution of the four-momenta experimentally obtained. To do so, the kinematic fit varies the measured parameters

within their errors to best fit a set of given constraints.
The mathematical procedure of kinematic fitting is shown below. This procedure can be performed in several iterations if necessary.

The vector $\boldsymbol{\alpha}$ represents the parameters for n tracks. A track describes the four-momentum and reaction vertex of a particle detected in the BGO ball. Typically each track has then seven parameters, the momentum in x-direction p_x, the momentum in y-direction p_y, the momentum in z-direction p_z, the energy E and the coordinates of the reaction vertex x, y and z. The initial parameters, obtained from the measurement are denoted $\boldsymbol{\alpha_A}$, while the initial parameters going into one iteration of the fit are called $\boldsymbol{\alpha_0}$.

$$\boldsymbol{\alpha} = \begin{pmatrix} \alpha_1 \\ \alpha_2 \\ \vdots \\ \alpha_\mathrm{n} \end{pmatrix} \tag{3.1}$$

Here $\boldsymbol{\alpha}_\mathrm{i}$ denotes the parameters of track i. From the errors σ_i of the initial measurement the covariance matrix $\mathbf{V_D}$ can be calculated.

$$\mathbf{V}_{\boldsymbol{\alpha_0}} = \begin{pmatrix} \sigma_1^2 & \left(\frac{\partial\sigma_1}{\partial\sigma_2}\right)^2 & \cdots & \left(\frac{\partial\sigma_1}{\partial\sigma_\mathrm{n}}\right)^2 \\ \left(\frac{\partial\sigma_2}{\partial\sigma_1}\right)^2 & \sigma_2^2 & \cdots & \left(\frac{\partial\sigma_2}{\partial\sigma_\mathrm{n}}\right)^2 \\ \vdots & \vdots & \ddots & \vdots \\ \left(\frac{\partial\sigma_\mathrm{n}}{\partial\sigma_1}\right)^2 & \left(\frac{\partial\sigma_\mathrm{n}}{\partial\sigma_2}\right)^2 & \cdots & \sigma_\mathrm{n}^2 \end{pmatrix} \tag{3.2}$$

Here $\left(\frac{\partial\sigma_\mathrm{i}}{\partial\sigma_\mathrm{j}}\right)$ denotes the dependence of the error of parameter i on the error of parameter j.

The r constraints of the fit are defined as functions $H(\boldsymbol{\alpha}) = 0$. The column vector $\mathbf{d}$ represent the constraints imposed on the fit, while $\mathbf{D}$ contains the derivations of the constraints with respect to the different parameters.

$$\mathbf{d} = \begin{pmatrix} H_1(\boldsymbol{\alpha}) \\ H_2(\boldsymbol{\alpha}) \\ \vdots \\ H_r(\boldsymbol{\alpha}) \end{pmatrix} \tag{3.3}$$

$$\mathbf{D} = \begin{pmatrix} \frac{\partial H_1}{\partial\alpha_1} & \frac{\partial H_1}{\partial\alpha_2} & \cdots & \frac{\partial H_1}{\partial\alpha_n} \\ \frac{\partial H_2}{\partial\alpha_1} & \frac{\partial H_2}{\partial\alpha_2} & \cdots & \frac{\partial H_2}{\partial\alpha_n} \\ \vdots & \vdots & \ddots & \vdots \\ \frac{\partial H_r}{\partial\alpha_1} & \frac{\partial H_r}{\partial\alpha_2} & \cdots & \frac{\partial H_r}{\partial\alpha_n} \end{pmatrix} \tag{3.4}$$

The constraint for momentum conservation in x-direction in the reaction $\gamma p \to \pi^0 p$ is e.g. written as

$$p^x_{\gamma_1} + p^x_{\gamma_2} + p^x_p = 0 \tag{3.5}$$

assuming the initial photon has no momentum in x-direction and the target proton is at rest.
After one iteration of the fit, during which the χ^2

$$\chi^2 = (\boldsymbol{\alpha} - \boldsymbol{\alpha_0})^T \mathbf{V_{\alpha_0}}^{-1} (\boldsymbol{\alpha} - \boldsymbol{\alpha_0}) + 2\lambda^T (\mathbf{D}\delta\boldsymbol{\alpha} + d) \tag{3.6}$$

of the fit is minimized with respect to $\boldsymbol{\alpha}$ and the *Lagrange multiplier* $\boldsymbol{\lambda}$ one obtains

$$\boldsymbol{\alpha} = \boldsymbol{\alpha_0} - \mathbf{V_{\alpha_0}} \mathbf{D^T} \boldsymbol{\lambda} \tag{3.7}$$

with

$$\begin{aligned}
\boldsymbol{\lambda} &= \mathbf{V_D}(\mathbf{D}\boldsymbol{\delta\alpha_0} + \mathbf{d}) && (3.8)\\
\mathbf{V_D} &= (\mathbf{D}\mathbf{V_{\alpha_0}}\mathbf{D^T})^{-1} && (3.9)\\
\mathbf{V_\alpha} &= \mathbf{V_{\alpha_0}} - \mathbf{V_{\alpha_0}}\mathbf{D^T}\mathbf{V_D}\mathbf{D}\mathbf{V_{\alpha_0}} && (3.10)\\
\boldsymbol{\delta\alpha_0} &= \boldsymbol{\alpha_0} - \boldsymbol{\alpha_A} && (3.11)
\end{aligned}$$

Here $\mathbf{V_\alpha}$ is the updated covariance matrix, $\mathbf{V_D}$ is an intermediate matrix used for the calculation and $\boldsymbol{\delta\alpha_0}$ is the change the parameter vector $\boldsymbol{\alpha_A}$ already underwent. Hence $\boldsymbol{\delta\alpha_0}$ is zero for the first iteration of the fit.
One can then calculate the χ^2 after the fit and convert this into a confidence level.

$$\begin{aligned}
\chi^2 &= \boldsymbol{\lambda}^T \mathbf{V_D}^{-1} \boldsymbol{\lambda} && (3.12)\\
&= \boldsymbol{\lambda}^T (\mathbf{D}\boldsymbol{\delta\alpha_0} + \mathbf{d}) && (3.13)
\end{aligned}$$

The confidence level ranges from zero to one and describes for each fit the probability that the fit yielded the correct results. If the errors of the measured parameters are estimated correctly, the distribution of the confidence level is flat. If the error are estimated too small, the distribution has a peak at zero, whereas too large errors lead to a peak at one. Another measure that indicates how well the fit performed is the *Pull*. It is calculated by

$$\sigma_j = \frac{\mathbf{D}_{ij}\boldsymbol{\delta\alpha_0}_i + \mathbf{d}_j}{\sqrt{\left(\mathbf{V_D}^{-1}\right)_{ij}}} \tag{3.14}$$

and shows how many standard deviations the parameter i had to be moved away from its initial value to fulfil the constraint j. For a working fit this distribution should be Gaussian around zero with a σ of one.

To test the kinematic fit, a well known and simple reaction channel will be used. For this work π^0 photoproduction was chosen, since the π^0 can already be reconstructed with a standard analysis.

3.9.1. π^0 photoproduction

At BGO-OD the π^0 is produced via photoproduction on a proton target. The produced pion subsequently decays almost exclusively into two photons (branching ratio $98.82 \pm 0.03\,\%$ [11]). Hence in the final state, two photons and the recoil proton can be observed.
For the future the fit will be tested on a more complex reactions such as the photoproduction channels $\gamma p \to \eta p$ or $\gamma p \to \eta' p$. Those are both channels that will benefit from the kinematic fit.
Finally the fit will be applied on the reaction $\gamma p \to K^0\Sigma^+$, where it will be essential to observe the reaction for a first time at BGO-OD.

4. The ARGUS detector

The ARGUS detector is a scintillating fibre hodoscope that complements the current BGO-OD tagging system. Its main purpose is to improve the resolution of the initial photon energy and thereby allow for finer energy binning of the initial photon energy in the energy range covered by ARGUS. This will generally improve and constrain the analysis' performed at BGO-OD, while it will be crucial for some reaction channels (e.g. $\gamma p \to K^0\Sigma^+$). It is also important to accurately characterize the coherent edge of a linear polarised beam, and hence extract the degree of polarisation. ARGUS was built in coordination with Björn-Eric Reitz.
This chapter starts with an explanation of the specific characteristics that ARGUS must have as well as the simulations, that were used to determine the optimal set-up to achieve said characteristics. Subsequently the tests that were performed on two prototypes to verify that the detector works are discussed. The chapter is concluded by giving the results of the operation of the full detector for a production run under normal beam conditions.

4.1. Requirements

ARGUS must improves the current tagger energy resolution. Additionally since it is a tagging detector, ARGUS must have an efficiency close to 100%, which essentially demands that all post-bremsstrahlung-electrons can be tagged.
Furthermore, there are spatial limitations to ARGUS. Since ARGUS must fit in front of the current tagger but behind the Møller polarimeter, there is only limited space available. Figure 4.1 shows the position of ARGUS in front of the tagger. These limitations are especially important for the PMTs and the readout electronics

4.2. Materials

The materials used for ARGUS were already chosen and delivered at the start of this thesis. To detect the post-bremsstrahlung electrons round scintillating plastic fibres having a diameter of 2 mm, manufactured by Saint-Gobain, are used [24]. Electrons passing through those fibres will create light through scintillation. To improve the trapping efficiency of this light the fibres have a double cladding.
The light pulses are read out by 16-channel Hamamatsu H6568 photomultiplier tubes [25], which have a fast anode rise time of 0.83 ns and only 1% crosstalk between the pixels. The most sensitive wavelength of the PMT is 420 nm and matches the 432 nm

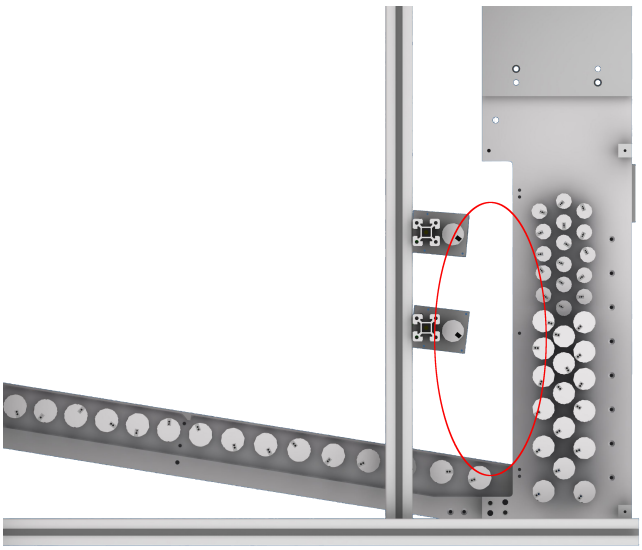

Figure 4.1.: Position of ARGUS in the current tagger set-up, denoted by the red oval. On the left the available space is limited by the Møller polarimeter.

wavelength of the scintillation light produced by the fibres.
One problem of the PMTs is that with high rate, the voltage of the last four dynodes becomes unstable. To avoid this problem the last four dynodes can be powered separately. Since it is not desired to have too many high voltage channels (due to cost efficiency and simplicity of the experiment), a high voltage card was specifically designed for the PMT, which provides high voltage for all dynodes including the last four. Using transistors, the card actively stabilises the voltage of the last dynodes and thereby increases the rate stability of the PMTs. Figure 4.2 shows a photograph of a card and the schematics can be found in appendix A.1.

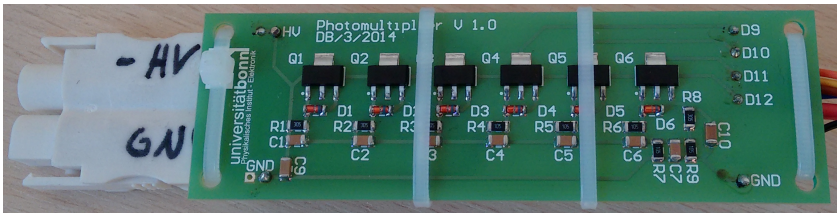

Figure 4.2.: High voltage card used to stabilise the high voltage of the last four dynodes of the PMT for high rates.

4.3. Characteristics

Before the detector can be constructed, there are characteristics that have to be determined, the most important one being the number of layers of scintillating fibres. Ideally there are as few layers as possible to simplify the construction of the detector as well as to maximize the region that can be covered with the given material. Since too many layers would give unnecessary redundancies, the possibilities of one, two or three layers were taken into account.
It is clear that only one layer of fibres is not a good option, since a single fibre does not have a detection efficiency of 100%. Furthermore, this set-up would be quite sensitive to thermal noise in the photomultiplier, as this could not be distinguished from a real electron. Furthermore, one faulty fibre would immediately result in a dead region of the detector.
What has to be determined is whether two layers are sufficient for good performance, or if three layers are needed.
Subsequently, it has to be determined if gaps between the fibres reduce the performance. In the final set-up these gaps can be created through glue between the fibres, so this question will have a great influence on how the mechanical holding structure of fibres and PMTs will look like.
The electrons have to pass a certain amount of material to give a valid signal (this is described in the next section). Figure 4.3 shows three layers of closely packed fibres with an incident electron. On the left the layers stand vertical, whereas on the right they are tilted. Comparing the left and the right side shows, that in certain cases some areas of the detector become inefficient because the electrons do not traverse enough material. These inefficiencies depend on the incident angle of the electron. Since ARGUS as well as the vertical part of the tagger are not located in the focal plane of the tagging magnet, the incident angle of post-bremsstrahlung electrons depends on the height, i.e. at which position the electrons hit the detector. Therefore, inefficiencies due to the incident angle are position related, which is not a desired effect, since it alters the obtained energy spectrum without any correlation to a physical process in the bremsstrahlung radiator. This problem can be avoided by tilting the detector, or at least parts of the detector. Whether this is necessary for ARGUS, has to be determined.

The properties above will be determined by conducting simulations with different set-ups. After this has been done, a mechanical holding structure can be devised, based on the simulation results and the spatial restrictions in the experimental area.

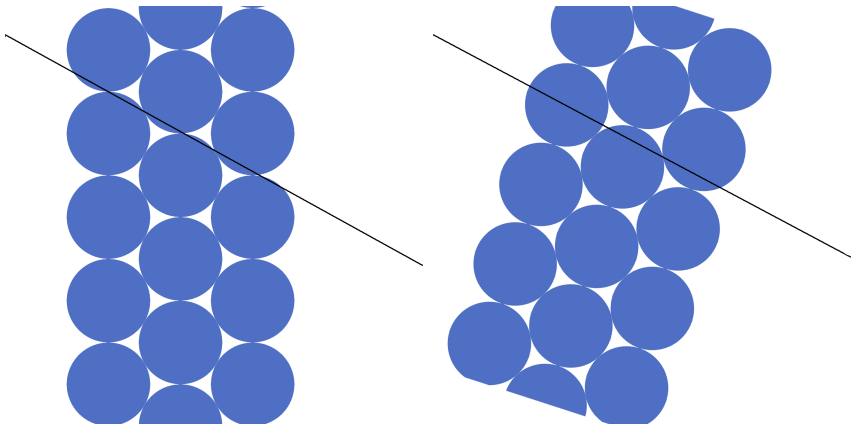

Figure 4.3.: Untilted and tilted array of fibres, with an incident electron illustrating the trajectories of post-bremsstrahlung electrons. For both cases the incident angle is similar. The right picture shows that tilting will in some cases increase the amount of material passed by the fibre and therefore the detection efficiency.

4.4. Simulation

To evaluate the properties of ARGUS, simulations were carried out with explora (see section 3.8). For the simulation, an array of overlapping scintillating fibres (like in figure 4.3) was endowed with the correct geometry and composition of plastic material and was positioned in front of the tagger. Configurations with two and three layers of overlapping fibres were tested.
To determine, whether or not an electron had traversed enough material to allow a fibre to scintillate and thereby register a hit, the electrons were assumed to be minimum ionizing particles. Thus their energy loss depending on the length of traversed material can be calculated by [11]

$$\frac{\mathrm{dE}}{\mathrm{dx}} = 2 \cdot \rho \cdot \frac{\mathrm{MeV} \cdot \mathrm{cm}^2}{\mathrm{g}}. \tag{4.1}$$

The fibres used have a density of $\rho = 1.05\,\mathrm{g/cm^3}$ and produce $n = 8000$ photons per MeV [24]. This means that the number of photons produced depending on the length of material the electron has travelled through can be calculated as

$$N'(x) = \frac{\mathrm{dE}}{\mathrm{dx}} \cdot n \cdot x. \tag{4.2}$$

Here x is the distance in cm. Not all photons produced will be trapped inside the scintillating fibre, so this number has to be multiplied by the fibre's trapping efficiency $\epsilon = 3.44\%$ [24]. Furthermore, the PMT has the standard quantum efficiency of $\epsilon_q = 20\%$

[25]. Taking into account the efficiencies, the number of photons detected by the PMT amounts to:

$$\begin{aligned} N(x) &= N'(x) \cdot \epsilon \cdot \epsilon_q & (4.3)\\ &= 114 \cdot x & (4.4) \end{aligned}$$

The statistical fluctuation on that number is $\sigma = \sqrt{N(x)}$. Assuming that a signal must be 3σ above the background to be recognized as an electron, it is possible to calculate the minimal length that must be traversed and the corresponding minimal deposited energy:

$$\begin{aligned} N(x) &> 3\sigma & (4.5)\\ \Rightarrow x &> 0.081\,\text{cm} & (4.6)\\ \Rightarrow \Delta E_{\text{min}} &= 170.1\,\text{keV} & (4.7) \end{aligned}$$

Hence for further analysis, only fibres are said to have given a signal, where the energy deposit is above 170.1 keV.

The method of *clustering* is used to reconstruct the position of the electrons in the detector. Because a hit in a single fibre is not sufficient to distinguish between background and a real electron, one can make use of the fact that an electron passing through the detector will hit several fibres, and so will induce signals in more than one fibre. Assuming that signals in adjacent fibres come from one particle, they can subsequently be grouped together into what is called a cluster. Therefore, the minimal size of a cluster is two. All possible positions for a cluster are numbered with an index, starting from one. Given how the fibre arrays are arranged along the vertical plane of the tagger, a lower number indexes a lower photon energy. Each such index is called a channel. Thus the channel of a cluster also gives its position. Figure 4.4 shows examples of what is and what is not a cluster.

The simulated electrons follow the spectrum of coherent bremsstrahlung, including the different coherent edges, as can be seen in figure 4.5. The energy ranges up to 3.2 GeV.

For every simulated set-up tested, resolution and efficiency for all channels were calculated. The efficiency could be calculated, by dividing the number of electrons the simulated ARGUS had registered at a certain index by the number of electrons that had actually passed this point in ARGUS. The resolution could be calculated by plotting the difference between the actual energy from the simulation and the energy measured by the ARGUS for every ARGUS channel. Fitting a Gaussian to that distribution ,a sigma can be extracted, which defines the energy resolution.
In reality it is possible, that some fibres or pixels of the PMT do not work or there is simply a bad connection between some fibres and their respective PMT pixel, resulting in an inefficient channel. To account for these inefficiencies as well as for any broken fibres, which do not give a signal, some broken fibres were put into the simulation.

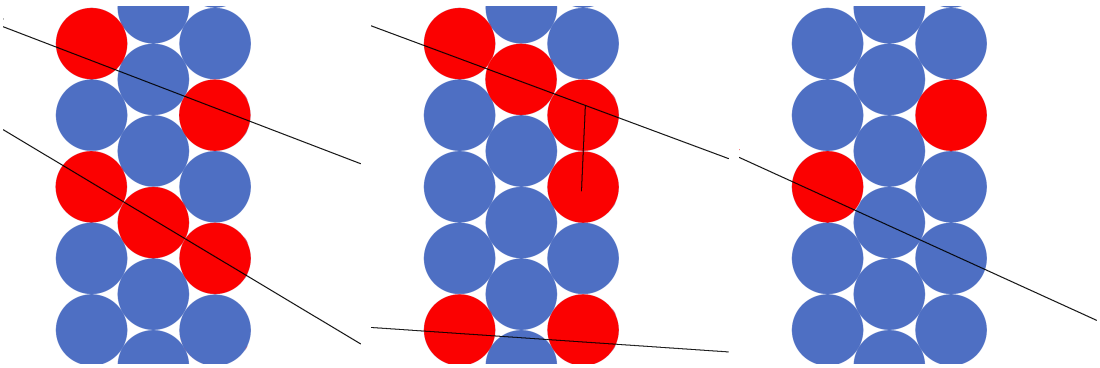

Figure 4.4.: Example of different arrangements of hit fibres in a three layered set-up: The black lines indicate incoming post-bremsstrahlung electrons, while the red fibres indicate fibres with a signal. The two configurations on the left are real clusters, which is also true for the two arrangements in the middle. The upper one has an additional δ-electron, that enhances the cluster. The pattern on the right is no real cluster, since it cannot be created by an incoming electron. It will therefore be treated as uncorrelated background.

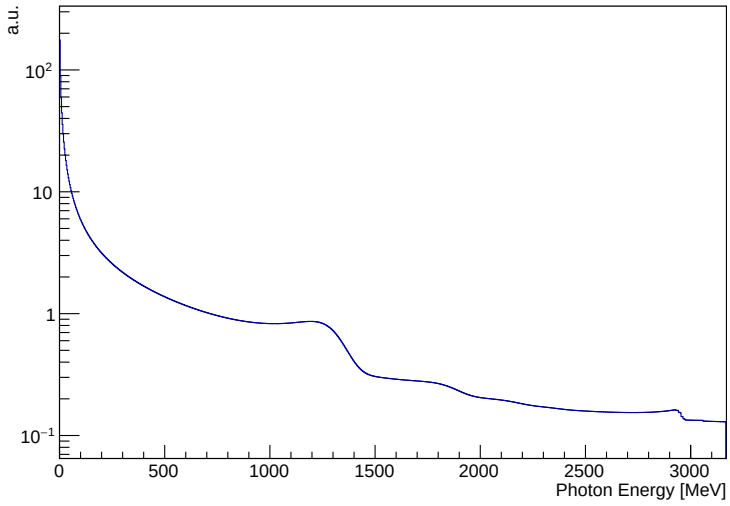

Figure 4.5.: Bremsstrahlung spectrum with a coherent contribution that was put into the simulation. The energy of the simulated electrons can be calculated by subtracting this from the ELSA energy. The y-axis is logarithmic for a better visibility of the coherent enhancements.

4.4.1. Two Layers

To test the layout with two layers of fibres, simulations with five million events each were carried out. For each event a post-bremsstrahlung electron was simulated with an energy calculated from figure 4.5. A simulation was performed for different tilt angles

$\psi = 0°, 10°, 20°$. Here ψ is the tilt angle as illustrated in figure 4.3. The angle of incidence for the post-bremsstrahlung electrons ranges from 8° to 20° for the vertical part of the tagger. Already included were 19 broken fibres. First of all, the efficiency of each set-up was checked to see if the efficiency has an angular dependence, figure 4.6 shows the simulated efficiency for each of the simulated angles.

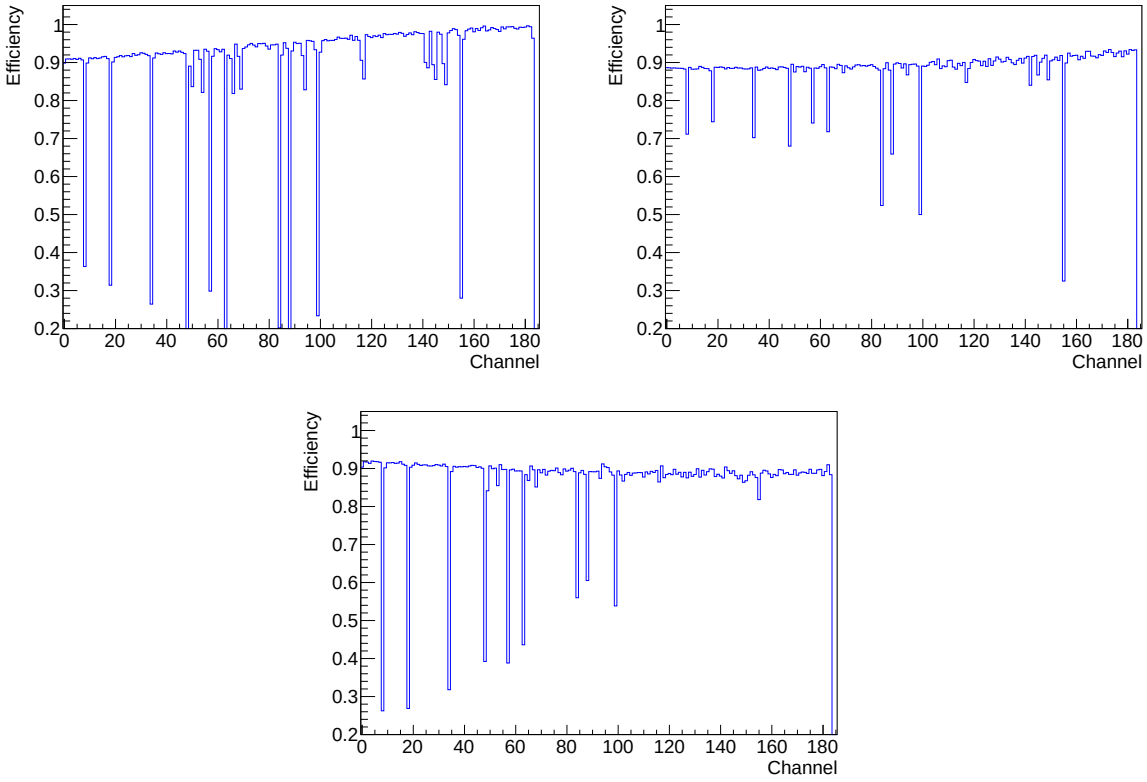

Figure 4.6.: Efficiencies for two layers of scintillating fibres with different tilt angles of ARGUS. Left to right, top to bottom: 0°, 10° and 20°. Each channel corresponds to one cluster index, as explained in section 4.4. This holds true for all other figures.

The efficiency for two layers of fibres is not in the range of 100%, but rather at approximately 90%. Additionally, the efficiency of the detector is not uniform over its whole range when there is no tilt of the detector. This is of course not desired, since a non-uniform efficiency will alter the observed spectra without any physical process in the radiator behind it. Also clearly visible are the effects of single damaged fibres, which reduce the efficiency down to approximately 20% for single channels.
For two layers it is therefore desirable to tilt the detector at approximately 10°. It remains to be seen if gaps between the fibres reduce the performance. Hence, the simulation for 10° was done again with gaps of 0.25 mm between the fibres. These gaps can be a result of glue between the fibres. The resulting efficiency can be seen in figure 4.7.

As can be seen from the plot, having gaps between the fibres is not beneficial, it

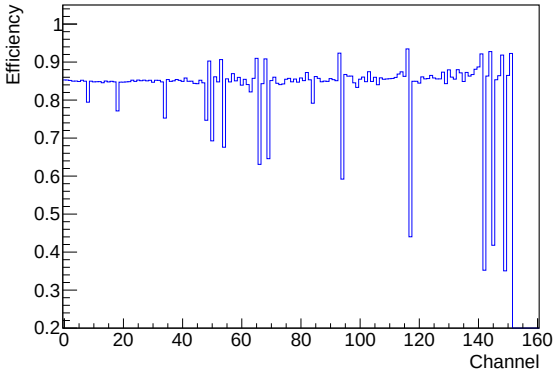

Figure 4.7.: Efficiency for a two-layered set-up with 0.25 mm gaps between the fibres.

reduces the overall efficiency by about 3% while the effects of broken fibres are more pronounced. Thus for two layers of fibres, the best configuration is to tilt the detector at approximately 10° and try to minimize gaps between fibres.
Figure 4.8 on the left shows the difference between the simulated energy and the measured energy. The discrete structure is an artefact of the discrete nature of the channels. By fitting a Gaussian to projections of this plot and extracting their σ, the resolution can be obtained. This is plotted in figure 4.8 on the right. Figure 4.9 shows the spectrum that can be obtained with this set-up. Again the effects of the broken fibres are clearly visible as the spectrum experiences gaps for single channels.

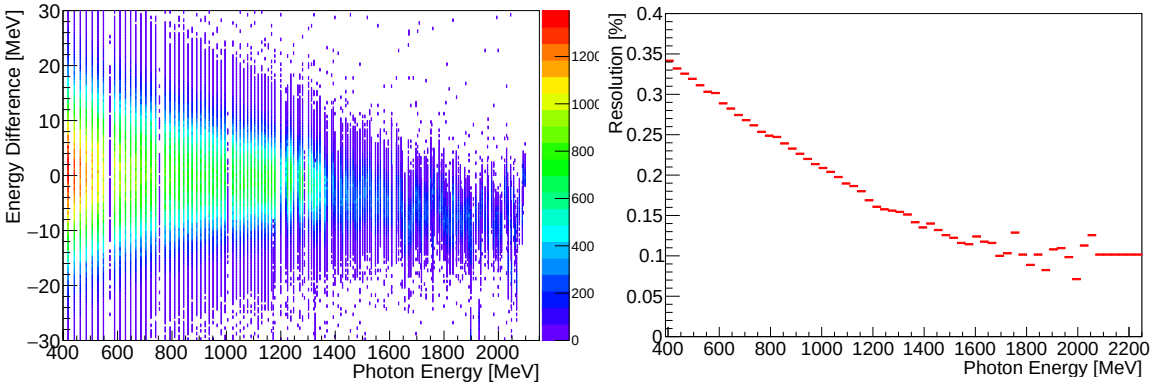

Figure 4.8.: Energy difference between the measured and the simulated photon energy (left) for a two layered set-up. Fitting Gaussians to projections of this histogram yields the respective resolution (right).

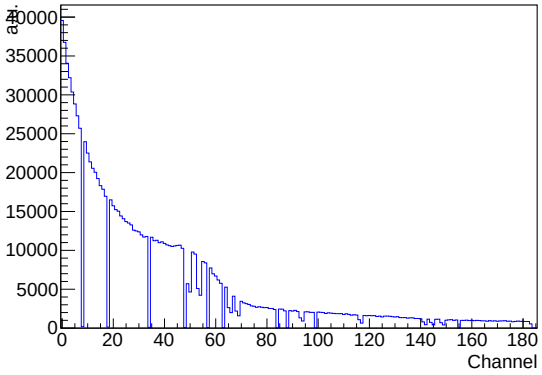

Figure 4.9.: Photon energy spectrum with coherent bremsstrahlung obtained from the simulation of ARGUS with two layers of densely packed fibres.

4.4.2. Three Layers

The same simulations were performed for three layers of fibres, including 33 broken fibres. Here it proved to be true that tilting the detector is not necessary, as can be seen in figure 4.10. The efficiency is close to 100% except for the channels with broken fibres. For those the efficiency drops to about 90% for the untilted detector. The bottom plot of figure 4.10 shows the effect of a decreased efficiency, due to a disadvantageous incident angle of the electrons. Around channel 130 the electrons have an incident angle, where they do not traverse enough material to create scintillation, as was explained in section 4.3.

Gaps of 0.25 mm were also simulated, but this time with no tilt. The resulting efficiency can be seen in figure 4.11. Evidently, the gaps reduce the overall efficiency, although not as much as for two layers. Nonetheless, this is not a desirable effect. Hence minimizing gaps is also a goal for three layers. The left panel in figure 4.12 shows the energy difference between simulated and measured energy, while on the right the obtained resolution is shown. Compared to the resolution obtained with two layers of fibres, the resolution for three layers has stronger fluctuations between the different channels. To understand those fluctuations one can look at the spectrum shown in 4.13. This is the energy spectrum obtained from the simulated ARGUS. Some channels count less events then their neighbouring channels, those low-count channels are related to broken fibres. The channels following those broken channels show a strong enhancement. These are events that were registered by ARGUS, but due to the broken fibre, their assigned position in ARGUS changed. Hence they are counted towards a higher channel. These electrons than tend to broaden this given channel, leading to the fluctuations in figure 4.12 on the right side. This effect does not occur for two layers, because a broken fibre mostly leads to a broken channel and not a shift in the cluster position.

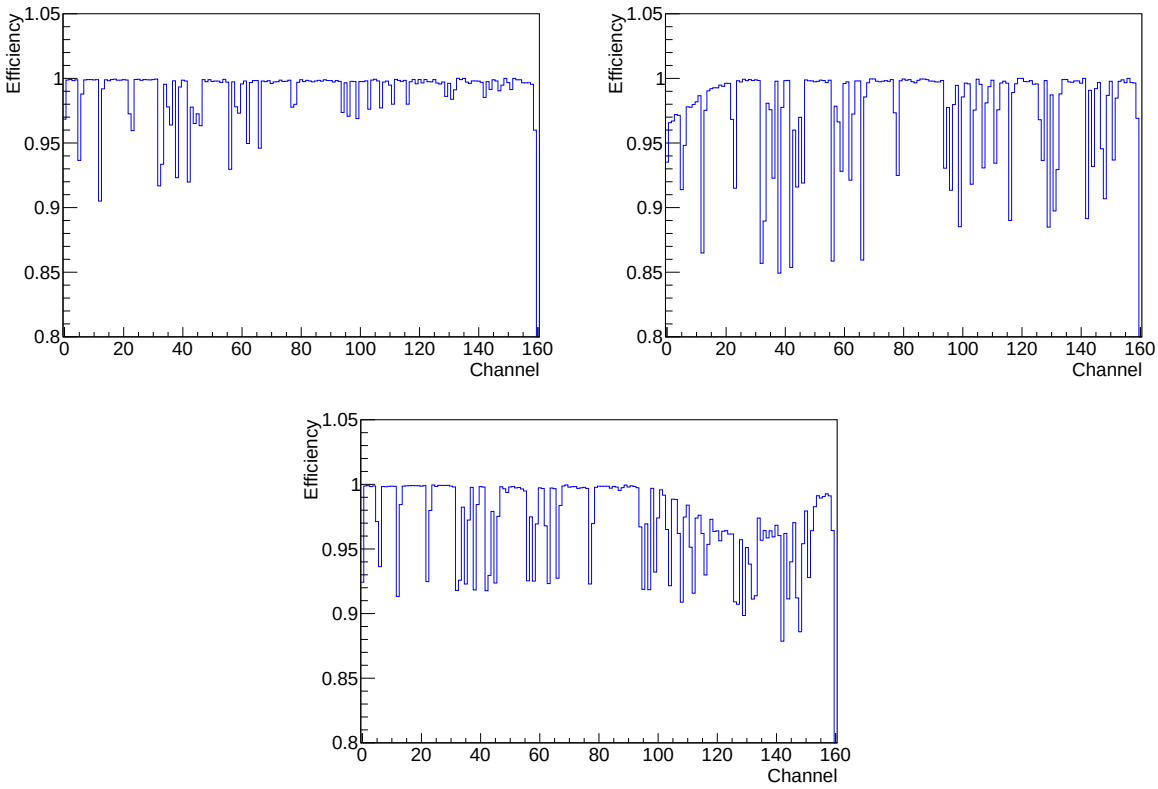

Figure 4.10.: Efficiencies for three layers of scintillating fibres with different tilt angles of ARGUS. Left to right, top to bottom: 0°, 10° and 20°.

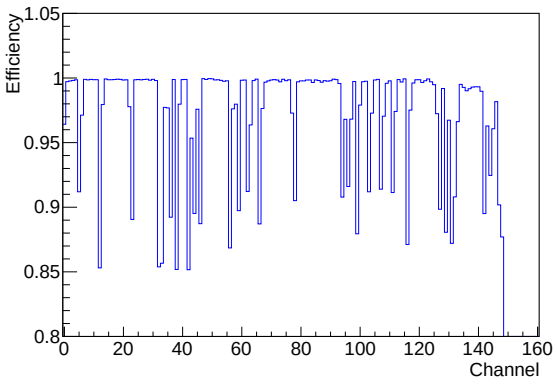

Figure 4.11.: Efficiency for a three-layered set-up with 0.25 mm gaps between the fibres.

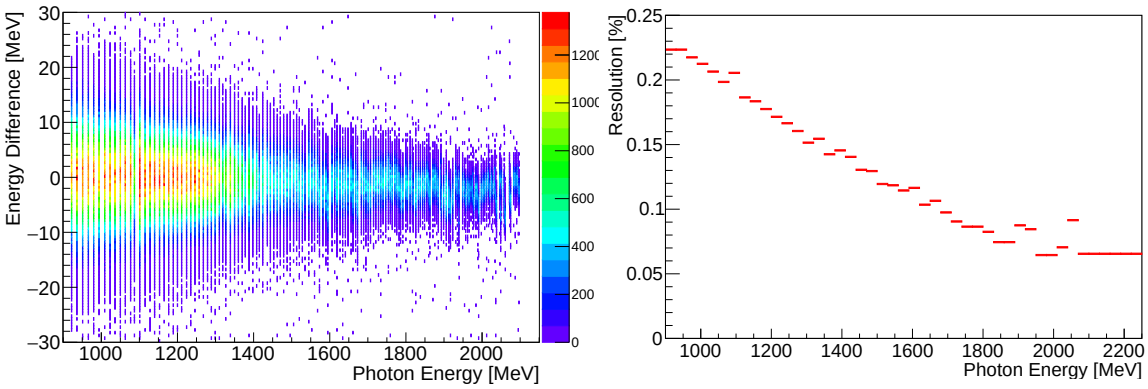

Figure 4.12.: Simulated energy difference between the measured and the real photon energy (left) for a three layered set-up. Fitting Gaussians to projections of this histogram yields the respective resolution (right).

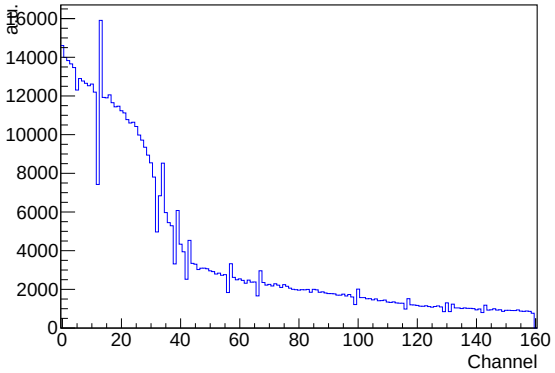

Figure 4.13.: Photon energy spectrum with coherent bremsstrahlung obtained from the simulation of ARGUS with two layers of densely packed fibres.

4.4.3. Conclusion

From the simulations it becomes evident that a design including three layers of fibres is a much more robust choice for a few reasons.
Demanding a cluster of size two decreases the background, since thermal noise etc. will only produce uncorrelated single signals. Whereas using the two-hit cluster size with only two layers leads to a decrease in efficiency (see figure 4.6), for the three-layered case there is no loss in efficiency (see figure 4.10). Hence a set-up with three layers rejects noise, while keeping the efficiency high. Moreover, the effect of broken fibres, or in general bad channels, is much less pronounced for three layers, as can be seen in the same figures.
Furthermore, the overall resolution is better for a set-up with three layers (see figure 4.8 and 4.12), providing an expected resolution of $(0.07 - 0.23)\% \cdot \mathrm{E}_0$ over an energy range of $(28 - 63)\% \cdot \mathrm{E}_0$.
Additionally, the simulations proved, that there is no need to tilt the detector, if three layers are used in order to improve its performance.
It was also shown that gaps between the fibres (e.g. from glue) must be minimized to optimise the detector performance.
The dependence between energy and channel in ARGUS can be seen in 4.14. When doing the energy calibration for the real detector, a similar correlation is expected.

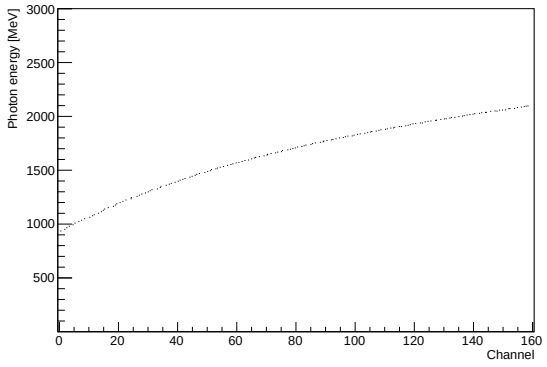

Figure 4.14.: Relation between the measured energy and the channel of ARGUS.

The results obtained from the simulations were subsequently used to built a prototype detector to test the results from the simulation as well as validate that the mechanical holding design works.

4.5. Prototype design

Since the simulation showed that having gaps between the fibres is not at all beneficial, one main goal of the holding structure was to avoid applying glue between the fibres. Therefore a robust mechanical harness holding the fibres tightly in place and thereby

minimize gaps between the fibres is required. The fibres were bundled in highly symmetric modules of 48 fibres that could be flipped or rotated to ease the construction and implementation. In the case of broken fibres another module can be inserted.
The full ARGUS detector was formed of 10 such modules, where each module contains three 16-channel PMTs which are connected to the respective 48 scintillating fibres.

As a first test, a prototype of one module was built. Unless otherwise mentioned, all the parts are made of aluminium to reduce the weight of the hardware. Figure 4.15 shows the set-up of one module. Additional pictures can be found in appendix A.2.

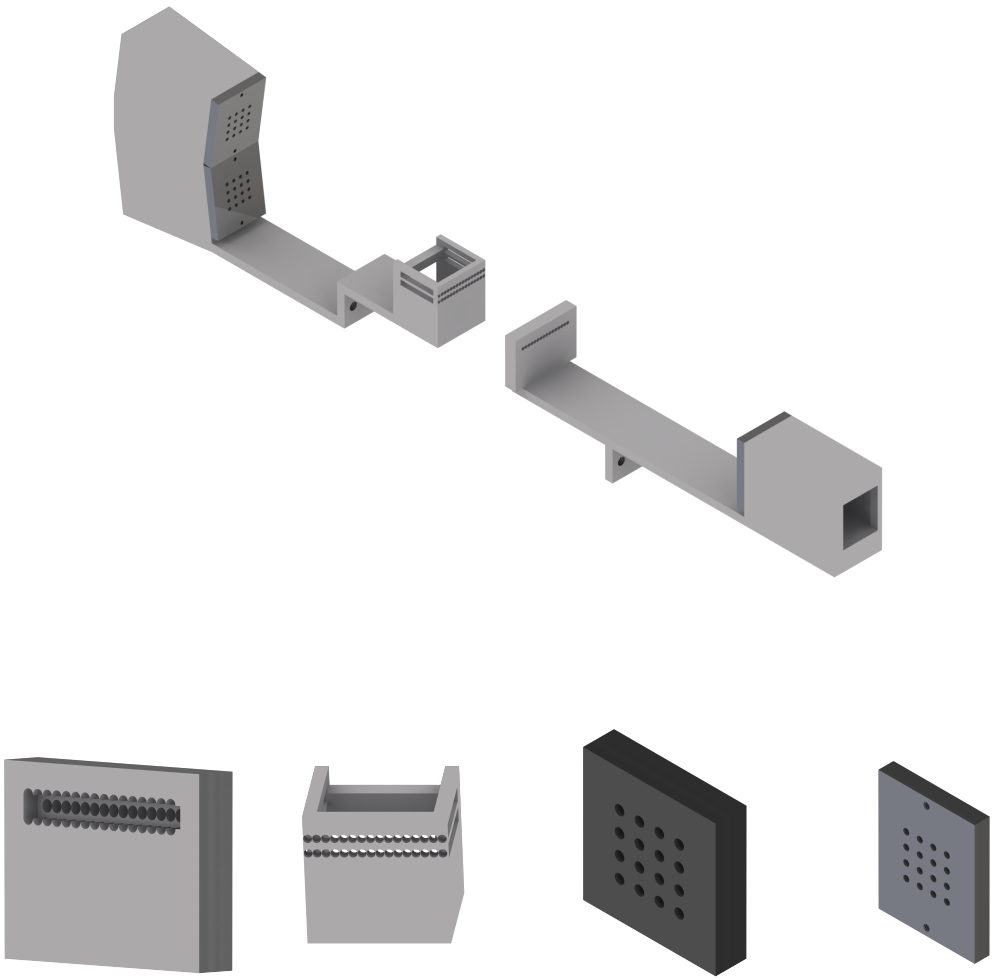

Figure 4.15.: Set-up of the first prototype. All pictures were taken with the graphical design program Inventor [34], which was also used to design these components. On the top is shown the mechanical holding structure of one module. The fibres in the middle and the PMTs in their housings are not shown. Depicted below are close-ups of different components. Going from left to right are the harness for the fibres on the side with one PMT, the fibre-harness on the other side, the PVC block in which the fibres are glued to press them on the PMT and lastly the cap that closes the PMT housing. These depictions of the components are not to scale.

Each PMT has sixteen pixels and consequently 16 fibres are attached to it. The ends of the fibres were glued into a block of PVC that is pressed on the PMT by a cap, also made of PVC, thereby coupling the fibres to the PMT. PVC was used to avoid damage to the PMTs and the fibres. To make sure that the coupling is as good as possible, the PVC block with fibres in it was smoothed using sandpaper of various strengths at the side which was pressed onto the PMT. Additionally, springs in the harness of the PMT apply pressure on this construction, such that there are no gaps between PMT and fibres, making for a solid contact.
Fibres from each PMT are arranged in one layer such that no fibres adjacent on the PMT are adjacent in the layers. This should prevent crosstalk between the fibres as well as on the PMT. The fibres are held in position by two mounts in the middle of the set-up. They each contain holes into which the fibres can be put through for maintaining their respective positions. As can be seen in the picture, one of the mounts is broader than the module itself. This means that this piece has to be redesigned for the final ARGUS detector. Also the holes in this mount do not go all the way through the material (see figure 4.15). Hence the fibres end inside the mount.
The housings and the mounts are screwed onto two T-beams that will subsequently be screwed onto the holding structure of the already existing tagger, see figure 4.16.

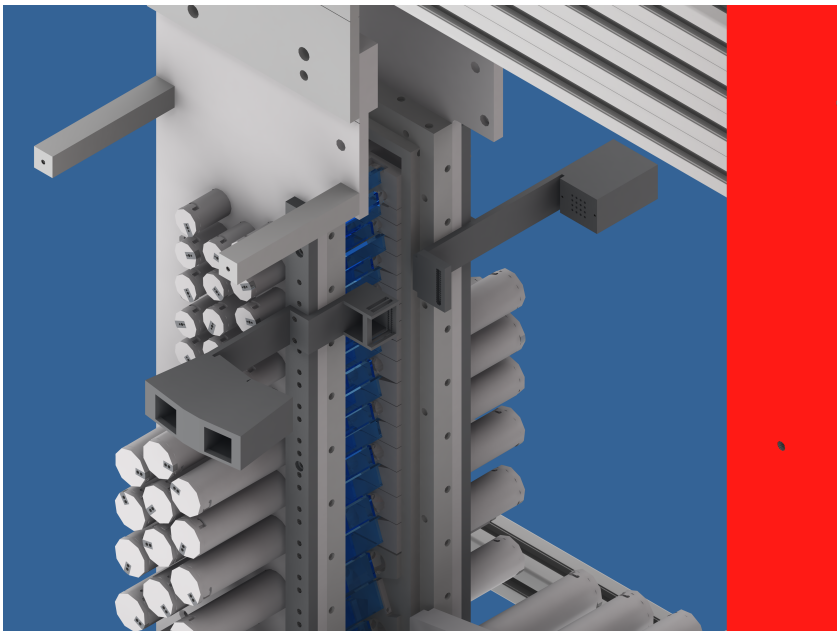

Figure 4.16.: The prototype module on the existing tagger. The figure does not show the fibres in the module.

On the side containing the two PMTs, the T-beam is bent down to make sure that the fibres coming from the upper PMT are bent as much as the ones coming from the lower PMT. Before the design phase, studies were performed to validate that bending fibres to the radii for this set-up would not hinder the performance of the fibres in guiding light to the PMT pixels. Furthermore, the bending of the T-beams proved to be necessary

in order to fit ARGUS between Møller polarimeter and tagger. The fibre length was chosen to be 20 cm.
The detector was made light tight by wrapping it in black foil and sealing the edges with black tape. Figures 4.17 and 4.18 show the module before and after it has been made light tight, respectively.
The readout of the photomultipliers was done via Spartan6 FPGA boards on which Time-over-threshold discriminator mezzanines were used. For every channel a threshold and a hysteresis can be set. Due to the limited space in the tagger area, the FPGA boards with the mezzanines on them were located in a rack, which was put on top of the beam dump.

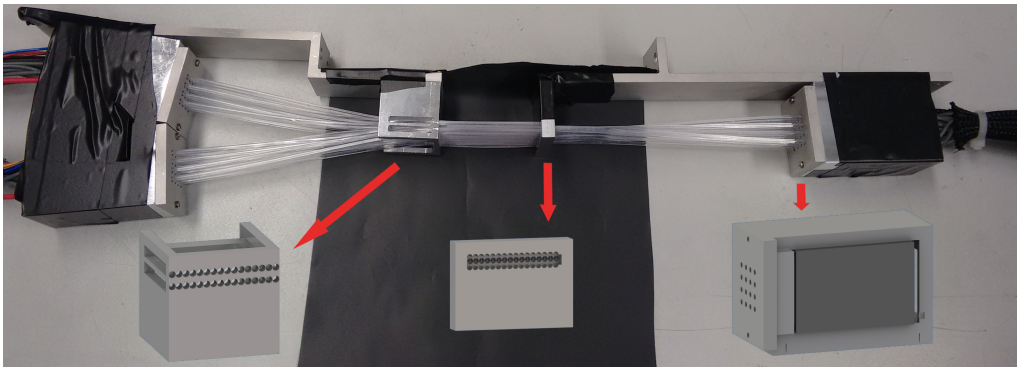

Figure 4.17.: Photograph of the prototype module. Also shown are graphics of the different parts, c.f. 4.15.

Figure 4.18.: Photograph of the prototype module with black foil around it, after being installed at the tagger. On the left the Møller polarimeter can be seen.

4.6. First Prototype test

The first prototype module was tested during a production run in March 2015. It was put in front of the tagger where it was read out during the normal operation of the experiment.
Before the detector could go into operation mode, however, threshold and hysteresis had to be set for every channel. The threshold had to be set in a way, that eliminates most of the background while leaving the signals mostly intact. The hysteresis is of additional help if the signals have a bad shape (see section 3.7). To determine the threshold necessary to eliminate background, an oscilloscope was connected to several channels. Subsequently signals from the channels without post-bremsstrahlung electrons hitting the detector were observed. Assuming that most of these signals come from background (since there is no bremsstrahlung), and only a few high are due to cosmic rays, one can set a first iteration of the thresholds by setting them to a value where nearly all background events are cut away. The threshold varies from channel to channel, but in general it was in the range of 35 mV to 100 mV. Hysteresis was kept around 15 mV.

The Time-over-Threshold (ToT) distribution of each channel was checked to fine tune the threshold. The left-hand side panel of figure 4.19 shows an example of such a spectrum. The peak at low ToT comes from background signals, as those will typically be not as high as real signals. The second peak at higher ToT stems from real signals. Hence for the fine tuning, parts of the low signal were cut away while also maintaining the real signals. Figure 4.19 on the right side shows the ToT spectrum for the same channel with adjusted thresholds.

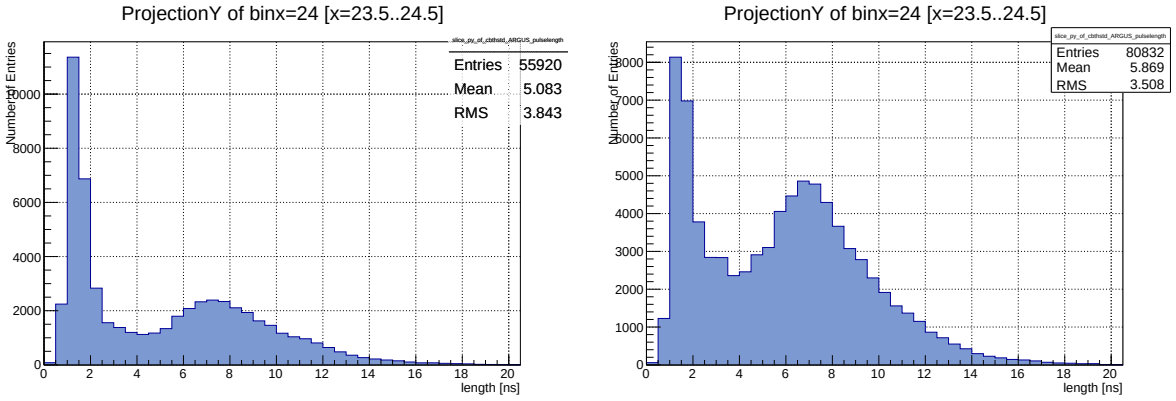

Figure 4.19.: ToT spectrum of one channel before (left) and after (right) the thresholds were adjusted. The enhancement of real signals with higher ToT is clearly visible. The different overall numbers are a result of the fact that these plots come from two different runs.

This operation was performed for each channel converging after several iterations. Hysteresis was also varied in the process of changing the thresholds, although it played a minor role. After setting the thresholds and hysteresis the detector was operational.

One of the main requirements for ARGUS was high efficiency. Hence, the efficiency of the prototype was measured by putting a 5 mm silicon detector in front of ARGUS, see figure 4.20. Requiring a coincidence between this silicon detector and the tagger region that is shadowed by said detector, it is ensured, that an electron has passed through this region. Therefore, the ARGUS efficiency can simply be calculated by dividing all coincidences between the silicon detector, ARGUS and the tagger, by the number of coincidences seen by silicon detector and tagger, since this is the total number of electrons that went through the ARGUS detector:

$$\epsilon = \frac{\text{Tagger \& Scintillator \& ARGUS}}{\text{Tagger \& Scintillator}} \tag{4.8}$$

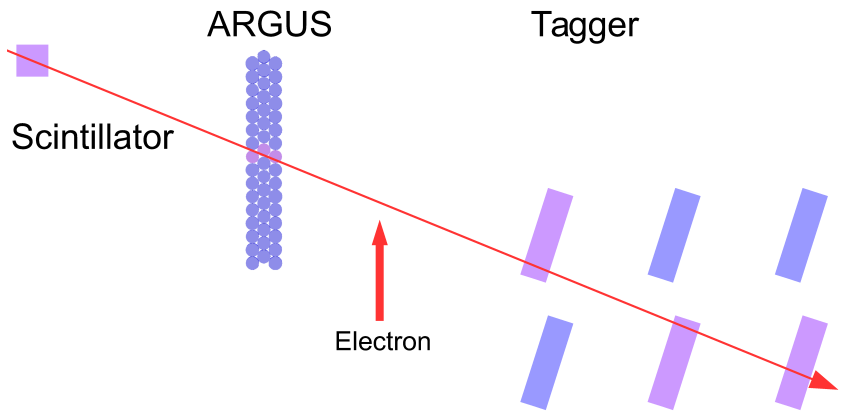

Figure 4.20.: Set-up for the ARGUS efficiency test. The fibres of ARGUS and the silicon blocks of the tagger and the small silicon detector, which show a purple colour have given a signal.

The efficiency was measured in this way for different rates by putting ARGUS at different positions along the tagger plane. This also measured the efficiency at different energies. The result of this test is shown in figure 4.21. It also contains the efficiency should one require only a single hit (single-hit response) and the probability to form a cluster around a single hit (intrinsic response).

The resulting efficiency was much lower than expected from simulation, as it was around 82%. Still this efficiency is constant with rate, which is a highly desired effect. Furthermore, the cluster building efficiency was around 95% meaning that building a cluster from the existing hits is seldom a problem, if there are additional hits. The single hit response was around 97%, meaning that mostly an electron was seen. Nonetheless, the events with only a single signal reduce the efficiency drastically. One reason for this could be bad connections between the fibres and the PMT.
After the beam time when the detector was dismounted it appeared, that at some point the fibres of the detector had become loose, see figure 4.22.

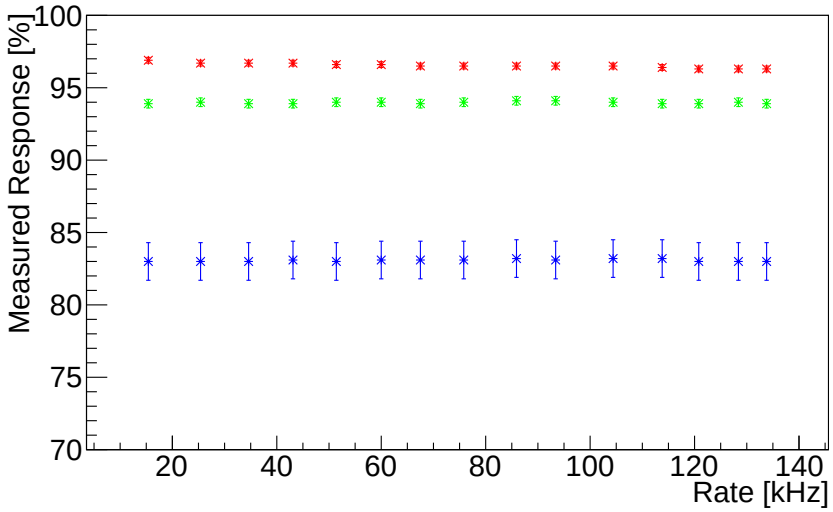

Figure 4.21.: Measured single hit response (red), multihit response (blue) and intrinsic response (green).

Figure 4.22.: Loose fibres after the first prototype test.

Since ARGUS was light tight before the installation in front of the tagger, it cannot be said at which point this happened, although it seems most probable, that the incident occurred when ARGUS was moved for the different efficiency measurements. The loose fibres created gaps between themselves and also disrupted the ordering of the fibres. Therefore this is another possible source of the low efficiency.
Additionally, it was tested, whether an aluminium plate in front of ARGUS would have any effect on the performance, in particular if it stops low energetic particles coming from the tagger. Such an effect could not be observed.

In conclusion the design for the first prototype proved to have some more flaws. First of all, it took the workshop a long time to manufacture the various parts and components,

especially the housings for the PMTs. Furthermore, it was not easy to remove a single PMT, which was one of the goals set for the design.
Due to these design flaws, as well as the low measured efficiency, it was decided to build an improved second prototype and test it again, before constructing the final detector.

4.7. Second prototype test

The second prototype test was done in April 2015. Again only one module was tested. Compared to the first prototype some changes were made:

- By separating the housings for the PMTs into various simpler parts, the construction for the workshop was simplified.
- The back part of the housing was replaced by a cap, thus making it easy to pull out a PMT without removing the whole module.
- The mounts for the fibres became longer with punching through holes on both sides, thus improving the stability and further making the assembly easier.
- The mount on the side with the single PMT now fits the width of the module.
- The PVC block for the fibres and the cap on it were merged into one PVC part.

Figure 4.23 shows the improved prototype. Additional pictures can be found in appendix A.3 and A.4.

The second prototype was put in during normal beamtime operation. Thresholds and hysteresis were set in the same manner as for the first test. The efficiency was measured in the same way as before, but only at one position and as it turned out the efficiency could be improved to about 95%. Due to this better efficiency, it was attempted to use ARGUS to measure the spectrum of the coherent edge, when using linear polarised photons. This turned out to be not possible, because one module does not cover enough energy to see the entire coherent edge. ARGUS is still very sensitive to the coherent peak. A clear enhancement can be seen in figure 4.24 when the coherent edge was shifted along the plane of ARGUS. This shows ARGUS' ability to see the coherent edge.

Apart from those operational improvements, the mechanical stability was also improved; no fibres became loose during this test. Additionally, the removal of single PMT turned out to be much easier and the whole set-up could be produced much faster. Due to those encouraging results, it was decided to stick with this design and produce 9 more identical modules for the final detector.

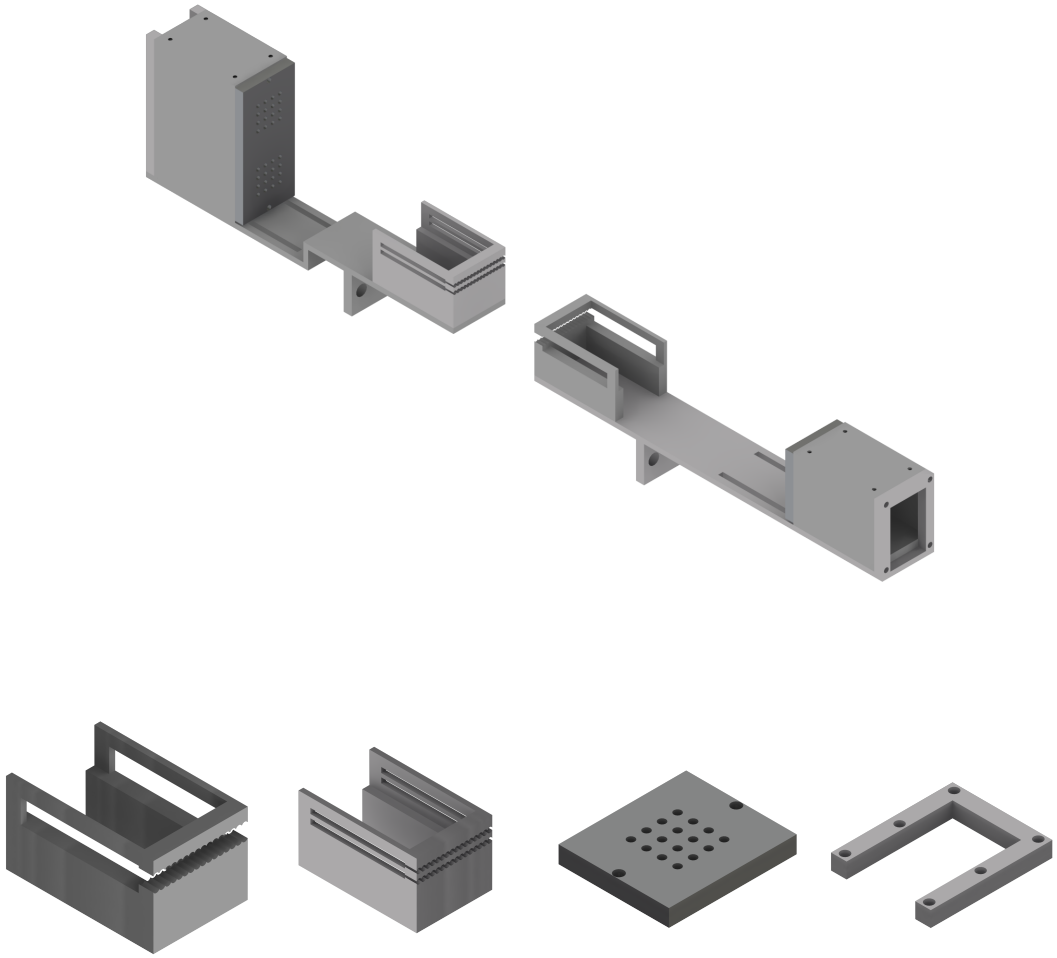

Figure 4.23.: Set-up of the second prototype. On the top is shown the mechanical holding structure of one module. The fibres in the middle, as well as the PMTs in their housings are not shown. Depicted below are close-ups of different components. Going from left to right are the harness for the fibres on the side with one PMT, the fibre-harness on the other side, the cap that also holds the fibres for the single-PMT-harness and the end-cap that closes the PMT-housing on the other side. The dents in the middle of the end-cap hold the springs that apply pressure on the PMT. These depictions of the components are not to scale.

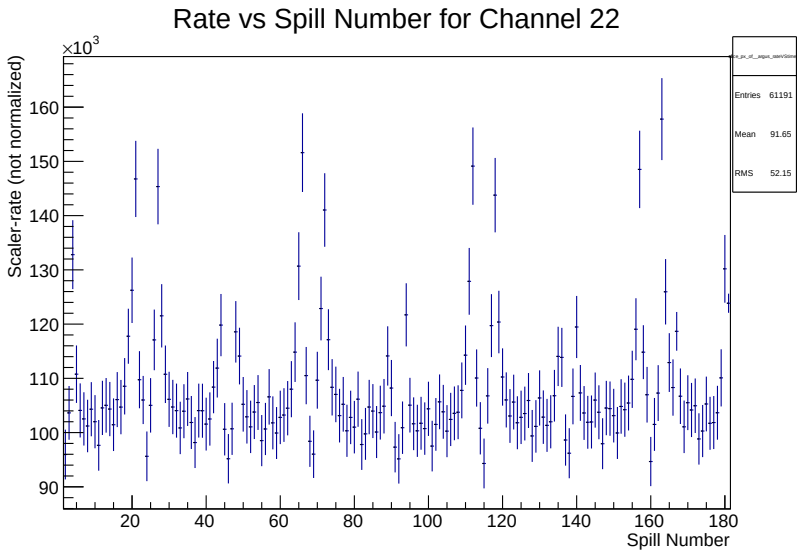

Figure 4.24.: Rate of ARGUS over time, when moving the coherent edge. The enhancements when the coherent edge moved over the detector can be clearly seen.

4.8. Final design and first full test

Since the second prototype test was successful, the final detector was made up from 10 identical modules. Due to delivery problems, the available readout electronics were only sufficient to read out half of the detector. Figure 4.25 shows a picture of the final detector. The detector was wrapped in black foil to make it light tight. In appendix A.5 additional pictures of the final detector can be found.

For the final detector a rough gain matching was done. For this procedure the lowest occurring gain of $3.30 \cdot 10^6$ was set to be the nominal gain. The voltage of that PMT was set to the nominal value of 800 V. Subsequently, the voltages from all other PMTs were varied such that their gain would match this nominal gain. Figure 4.26 shows the relation between voltage and gain that was used for the procedure. Appendix A.1 lists all PMT gains and the respective voltages.

Following the gain matching, the thresholds and hysteresis were set using the same method as for the two prototype tests. Tables A.2 to A.6 in the appendix show a list of all thresholds and hysteresis. The efficiency was checked again to make sure that the assembly was successful. The results were again excellent, giving an efficiency of 95%.

In principle the detector was now operational. However one would still only obtain the position of the post-bremsstrahlung electron from ARGUS and no information about the energy of the produced photon. Hence an energy calibration has to be performed, which links each channel to a respective photon energy, such that the position information is linked to the energy of the produced photon.
The trajectories of the post-bremsstrahlung electrons are bent due to the Lorentz force $|\vec{F_L}| = q \cdot |\vec{v} \times \vec{B}|$. The velocity of the electrons can be expressed through their momentum and since the electrons are relativistic their momentum is equal to the energy. Thus the Lorentz force is proportional to the energy of an electron as well as the magnetic field of the tagging magnet.
Due to the fact that the force is linear in B and E, the field B_{ch} necessary to bend the primary beam in a certain channel is given as

$$B_{ch} = \frac{E}{E_{ch}} \cdot B. \tag{4.9}$$

where E is the energy of the primary beam used for calibration, e.g. the ELSA energy, and B is the corresponding nominal field value of the tagger magnet. E_{ch} is the energy assigned to the channel, i.e. the value that has to be determined. It is the energy an electron has to have to be bent into that specific channel under nominal field B. From the above equation the relative energy of every channel can be calculated by means of

$$\frac{E_{ch}}{E} = \frac{B}{B_{ch}} \tag{4.10}$$

$$. \tag{4.11}$$

Figure 4.25.: Photographs of the final detector. The top row shows photographs of the fibres of the final detector set-up. The bottom picture shows the light tight ARGUS at its final position in front of the tagger.

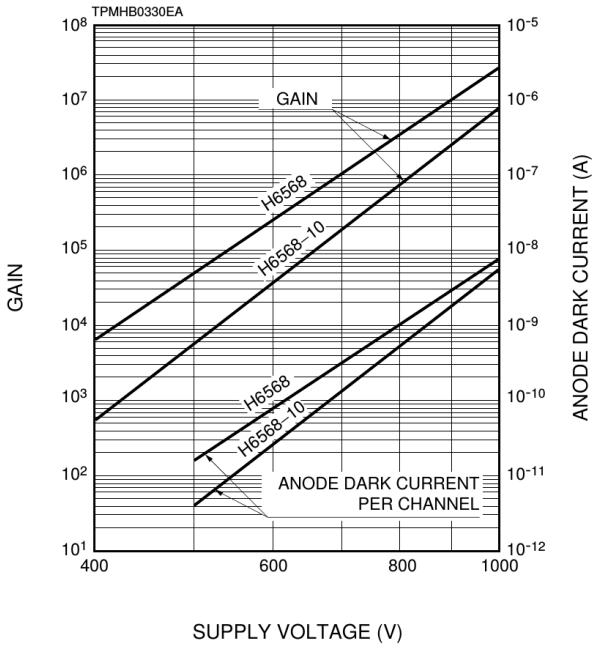

Figure 4.26.: Typical gain and anode dark current for the used photomultipliers [25].

What remained to be determined is the field value B_{ch} corresponding to every channel. To perform this calibration procedure, the primary beam was swept over the detector using a low intensity electron beam of 0.05 pA. The nominal intensity is of the order of 1000 pA. This low intensity was necessary so as to not damage the ARGUS detector in the process. No radiator was used since only the primary beam should be bent and no electrons that would undergo bremsstrahlung.
The sweeping was done by varying the field of the dipole magnet. Since electrons of a given momentum will be bent less for decreasing magnetic field, the primary beam will thereby sweep across the plane of ARGUS. This then results in a plot like figure 4.27 for each channel. This is a distribution of the number of hits measured in a certain channel depending on the magnetic field. Since only half the detector could be read out, the calibration was performed in three steps, each time reading out a different part of ARGUS. The regions covered in the three steps had a certain overlap to avoid gaps in the calibration.

Fitting a Gaussian function to these distributions, the field B_{ch} necessary to bend an electron to this channel could be calculated. It is the mean of the Gaussian distribution. Using equation 4.11, E_{ch} could be extracted. The result of the energy calibration can be seen in figure 4.28 on the left. On the right the energy width of each channel is shown. It can be calculated by

$$\frac{\Delta E}{E} = B \cdot \left(\frac{1}{B_{ch} - \Delta B_{ch}} - \frac{1}{B_{ch} + \Delta B_{ch}} \right) \tag{4.12}$$

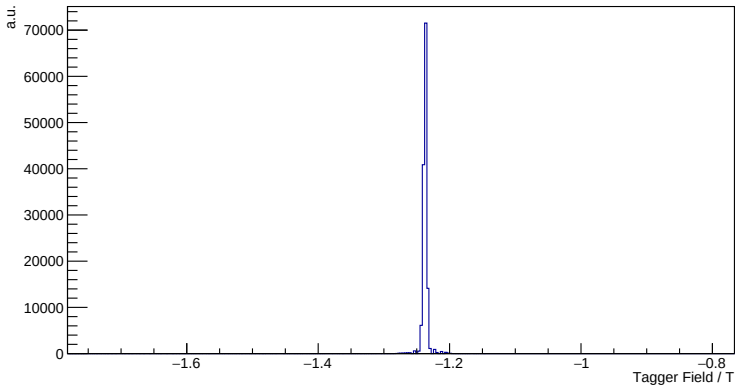

Figure 4.27.: Dependency of the counts in one channel on the magnetic field.

where ΔB_{ch} is the width of the distribution shown in figure 4.27, e.g. the sigma of the fitted Gaussian. Since the beam used for the calibration had a mean width of approximately 4 mm, which was wider than the individual fibres, the calculation of the energy width was less reliable, which can be seen in the fluctuations in figure 4.28 on the right.

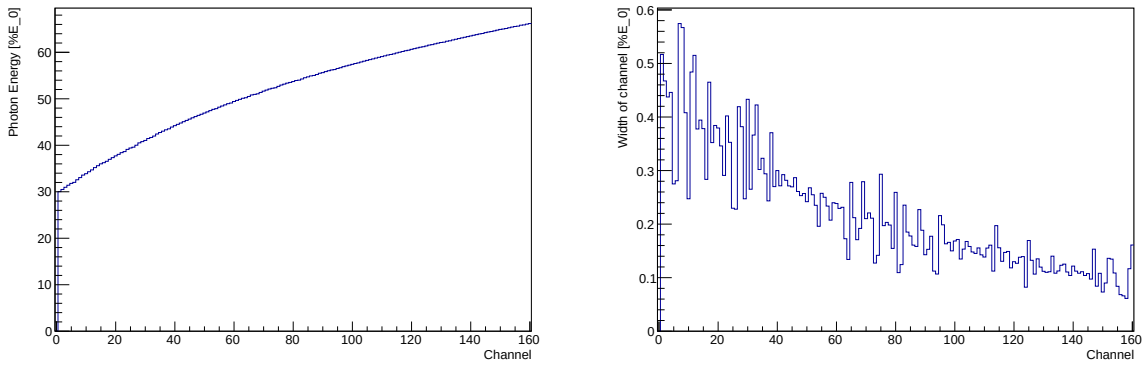

Figure 4.28.: Energy per channel and energy width per channel obtained from the energy calibration. The fluctuations in the energy widths of the channels are due to the fact that the beam is broader than the individual channels.

The obtained energy resolution is $(0.08 - 0.45)\% \cdot \mathrm{E}_0$ over an energy range of $(30 - 66)\% \cdot \mathrm{E}_0$. The resolution is slightly worse than the $(0.07 - 0.23)\% \cdot \mathrm{E}_0$ expected from the simulation.

Figure 4.29 shows the corresponding results for the existing tagger. As can be seen, the resolution is improved by more than the desired factor five. The left panel in 4.29 shows the electron energy for each tagger channel. This is in agreement with the photon energy per channel obtained from ARGUS.

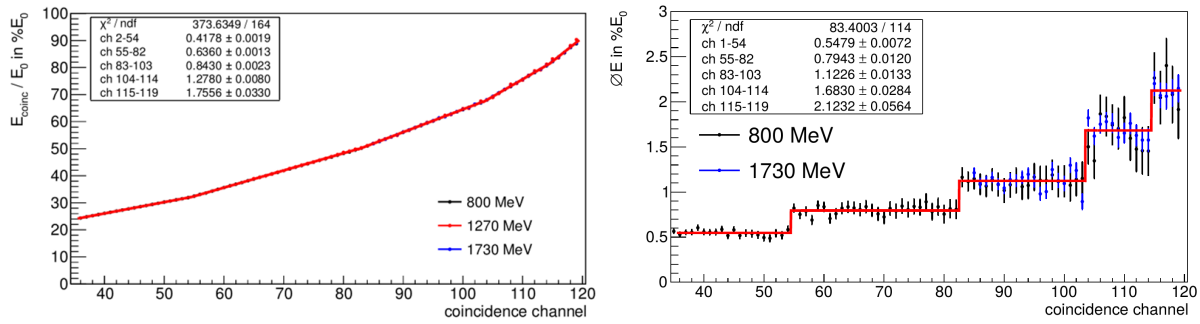

Figure 4.29.: Energy calibration for the tagger with corresponding width for the energy channels on the right. For the tagger the calibration was performed with several energies.

With a bigger part of the detector operational, it was possible to cover a bigger part of the coherent edge, see figure 4.30, such that coherent edge could be measured. As can be seen from the same figure the shape agrees well with what was measured with the tagger.

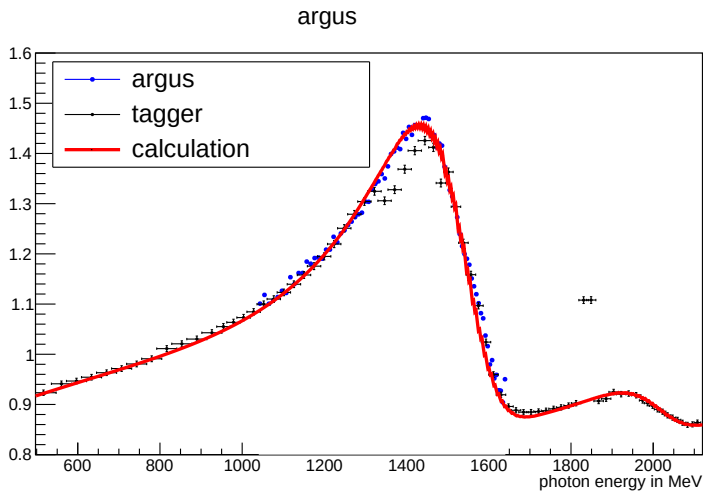

Figure 4.30.: Energy spectrum over the coherent edge taken with the tagger and with ARGUS. The plot shows the coherent spectrum divided by the incoherent one.

Thus half of the ARGUS detector was fully operational for this beam time and could be used for data taking and later on for the different analyses. Upon the arrival of the missing components of the readout electronics, the full ARGUS will become operational.

5. The kinematic fitting

With ARGUS being operational, the resolution of the initial beam energy and the incident four-momentum has been improved. This was an improvement made on the hardware of the experiment.
Improving the current analysis software by using a kinematic fitting algorithm is essential to enhance the resolution of the four-momenta of the particles in the final state and make certain reaction channels visible for the first time (e.g. $\gamma p \to K^0\Sigma^+$). The kinematic fit will also verify that the energy calibrations and positions of all detectors are correct and the resolutions of the measured parameters (i.e. the errors) are correctly estimated. To test the kinematic fit, the fit was applied on a simple, already observed reaction. This way, by comparing the results from the fit to the results from a standard analysis, it can be verified that the fit works in general and most importantly that it increases the resolution. The reaction $\gamma p \to \pi^0 p$ was chosen for this purpose.
This chapter will briefly show the results, which can be obtained by a standard analysis (e.g. combining the four vectors of the measured particles). Subsequently the results of the kinematic fit in comparison to the standard analysis are shown.

5.1. Standard analysis

In the standard analysis the four-momenta of the two decay photons p_{γ_i} were combined to form the four-momentum of the pion p_{π^0}.

$$p_{\pi^0} = p_{\gamma_1} + p_{\gamma_2} \tag{5.1}$$

Before this could be done, the particles had to be identified. In order to do this, the information obtained from the BGO ball and the barrel around the target were combined to a track. This track gets its direction from the θ and ϕ angle obtained from the BGO ball as well as the hit position of the barrel. The kinetic energy E of the track/particle equals the energy deposited in the BGO ball. If the particle is charged, it produces a hit in the barrel. If not, there is no signal in the barrel. This determines whether the particle was charged or not. This information is consequently assigned to the track.
Depending on the charge the tracks were either called a proton or a photon. The tracks were then assigned a charge and a four-momentum based on the chosen hypothesis. The four-momentum was calculated from the measured parameters (θ, ϕ and E).
Since the π^0 decays into two photons, only such events were taken into account where the number of photons is two. Furthermore the energy of the corresponding initial photon had to be be above 144.685 MeV, which is the threshold to produce a π^0 on a proton

target. This initial energy was taken from ARGUS for the energy region covered by the detector, for the rest of the energy spectrum the energy of the initial photon was taken from the tagger. In this way an optimal energy resolution could be obtained over the whole range of the energy spectrum. A proton detected in the BGO ball was also required.
The two photons were now combined to form a π^0. Figure 5.1 shows a distribution of the invariant mass, calculated from the four-momenta (see equation 5.1).

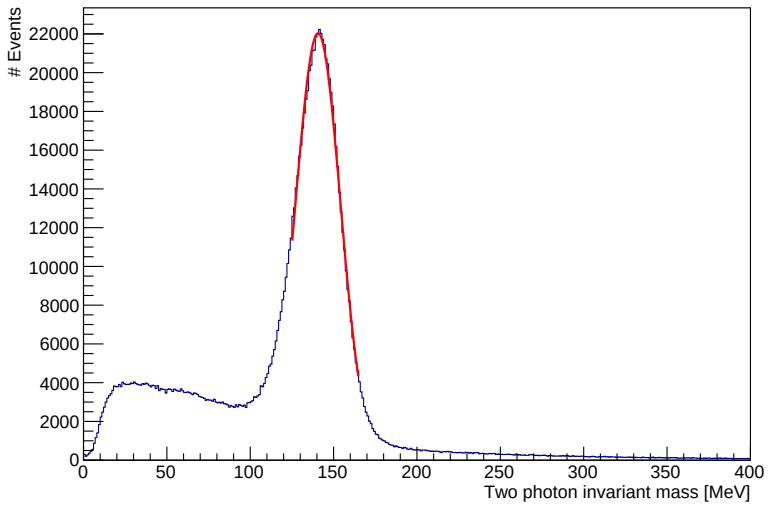

Figure 5.1.: Invariant mass of the two photons, clearly visible is the π^0 peak. The results of the fit are shown in table 5.1.

The reconstructed π^0 are clearly visible with a peak close to the expected pion mass of 134.9776 MeV [11]. Still there is some background below the pion-peak. This background results from combinations of two photons that did not originate from a π^0 decay. There are two reason why this can occur:

- There were more then two photons in the event, but only two got detected. Those two did not come from the same π^0.
- One of the photons was actually another particle and was wrongly identified as a photon.

Since the initial photon energy E_0 is known, the missing mass m_{miss} could be calculated as:

$$m_{miss} = \sqrt{p_0 + p_{target} - p_{\gamma_1} - p_{\gamma_2}} \tag{5.2}$$

Here p_{target} is the four-momentum of the target, since it is at rest this is just the mass of the target, i.e. the proton mass. p_0 is the four-momentum of the initial photon. The missing mass is expected to be located at the proton mass, if the reaction is $\gamma p \to \pi^0 p$. Figure 5.2 on the left shows the invariant mass of the two photons versus the missing mass, the right panel shows the missing mass distribution. Most events are located at the π^0 and proton mass, as is expected from the chosen events.

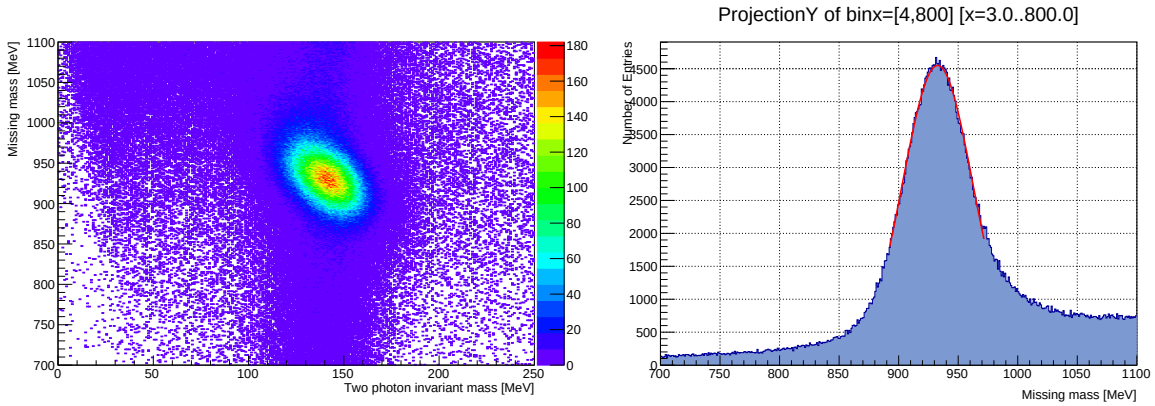

Figure 5.2.: Invariant mass of the two photons versus missing mass (left) and distribution of the missing mass (right).The parameters of the fit can be found in table 5.1.

By fitting Gaussians to the invariant mass distribution, as well as the missing mass distribution, the mean values and the σ for those parameters could be extracted, table 5.1 shows the results.

Parameter	Mean [MeV]	σ [MeV]
Invariant mass	140.65 ± 0.03	13.39 ± 0.03
Missing mass	932.72 ± 0.08	29.56 ± 0.12

Table 5.1.: Mean and σ of the invariant mass distribution of two photons and the missing mass calculated. The errors are the errors of the fit.

As can be seen, the pion mass is slightly off from the nominal value of 134.9776 MeV, the missing mass (which should be the proton mass) is also too low ($m_{proton} = 938.272$ MeV [11]). These effects originate from an incorrect first energy calibration of the BGO-OD. A better energy calibration is under work.

5.2. Analysis with the kinematic fit

As could be seen in the previous chapter, the extracted pion and proton masses are incorrect, due to an incorrect energy calibration. This will definitely lead to wrong pull distributions after the fit, since the fit has to fulfil the given constraints with wrong

parameters. For this work the fit was performed without correcting the calibration first. Hence the results of the fit will be strongly affected by this problem and have to be seen as very preliminary.
To perform the fit the mathematical procedure shown in 3.9 was applied. The input parameters were the four-momenta of the two photons together with the proton four-momentum. Additionally for each particle three parameters x, y and z were introduced. Those specify the point of origin for those particles, i.e. for the photons this is the point were the π^0 decayed and for the proton this is the reaction vertex. For the given detector accuracies those two are the same. Since there is no knowledge on the exact origin of the particles, it is assumed that they all come from the centre of the target, i.e from $(x, y, z) = (0, 0, 0)$. These parameters are not important for the current fit, but when the fit is applied to more complex reaction channels, these parameters can be used as additional constraints.
The errors of the fit parameters had to be calculated from the errors of the measured parameters ϕ, θ and E. The errors in ϕ and θ depend not only on the BGO ball performance, but also on the size of the target and the size of the beam spot. The beam spot also yields the errors in x and y, while the z error equals the target length divided by π. This approximates a Gaussian distribution for the target length, which is necessary for the correct errors.

The constraints used for this fit are momentum conservation in the x-y plane. Since the z-direction of the experiment is defined as the direction of the produced photon beam, the x-y plane is the plane perpendicular to that direction. The initial photon has no momentum in the x-y plane, therefore those terms can be neglected.

$$p^x_{\gamma_1} + p^x_{\gamma_2} + p^x_p = 0 \tag{5.3}$$
$$p^y_{\gamma_1} + p^y_{\gamma_2} + p^y_p = 0 \tag{5.4}$$

The left panel in figure 5.3 shows the χ^2 distribution of the fit. For a fit where the parameters have the proper errors and also the calibrations are correct, this distribution should have its mean at one. As can be seen from the figure, this is not the case for the current fit. This is most probably a result of the incorrect BGO ball calibration.
The right panel of figure 5.3 shows the confidence level obtained from the χ^2. This distribution has a concise peak at zero. These are events where the fit was not able to fulfil the constraints within the given errors. Hence these events have to be disregarded for the rest of the analysis. Ideally the distribution of the confidence level should be flat.

An additional measure of how well the fit performed is the pull-distribution. The pull of all parameters with respect to the momentum conservation in x-direction can be seen in figure 5.4 on the left side. The right side of this figure shows the pull-distribution for the proton momentum in x-direction p^x_p.

As was explained earlier the pull should have a Gaussian shape and be centred around zero with a σ of one. After this fit the pull-distributions of all parameters are centred around zero, except for $p^x_{\gamma_1}$. Nonetheless the pull-distribution of p^x_p shown on the right

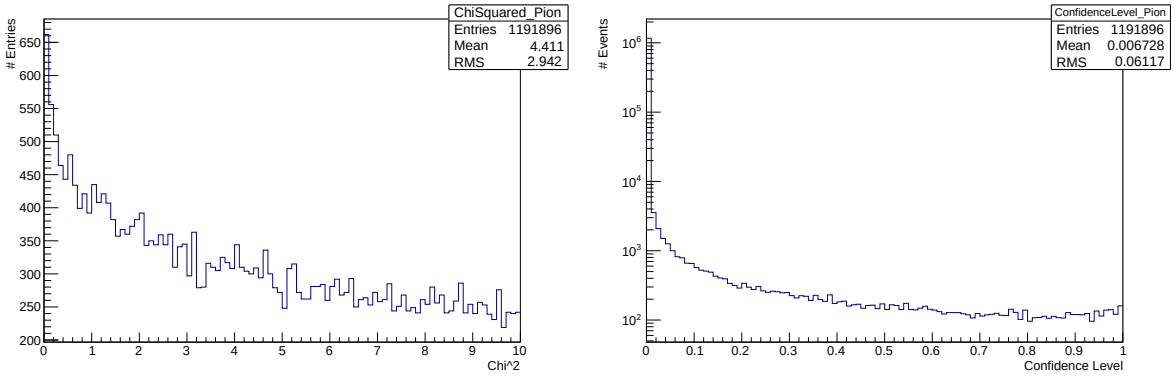

Figure 5.3.: χ^2 (left) and confidence level (right) distribution for the performed kinematic fit. The scale of the confidence level is logarithmic for better visibility of the distribution.

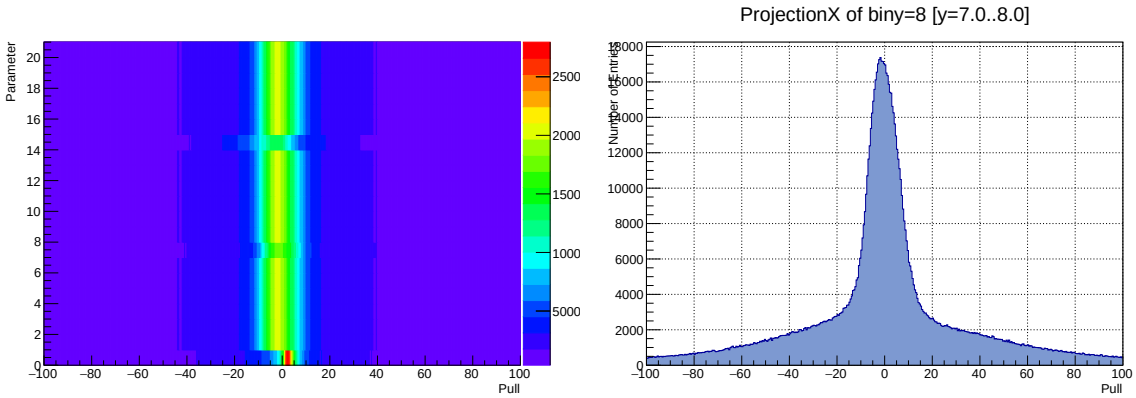

Figure 5.4.: Pull-distribution for all parameters (left) and one single parameter (right). The pull is calculated with respect to the x-direction momentum conservation. The numbers on the y-axis of the left plot indicates the different parameters: $0 = p^x_{\gamma_1}$, $1 = p^y_{\gamma_1}$, $2 = p^z_{\gamma_1}$, $3 = E_{\gamma_1}$, $4 = x_{\gamma_1}$, $5 = y_{\gamma_1}$, $6 = z_{\gamma_1}$, $7 = p^x_p$ etc.. Therefore the pull-distribution on the right belongs to p^x_p.

of figure 5.4 is not Gaussian and has a σ much wider than one. This is also true for all other distributions and again emphasises the problem with the energy calibration. This was already indicated through the χ^2 distribution.

Nevertheless this thesis will show the results obtained with the fit at its current stage. The invariant mass spectrum of all fits with a confidence level higher than 0.015 can be seen in figure 5.5 on the left side. On the right the invariant mass is plotted versus the missing mass.

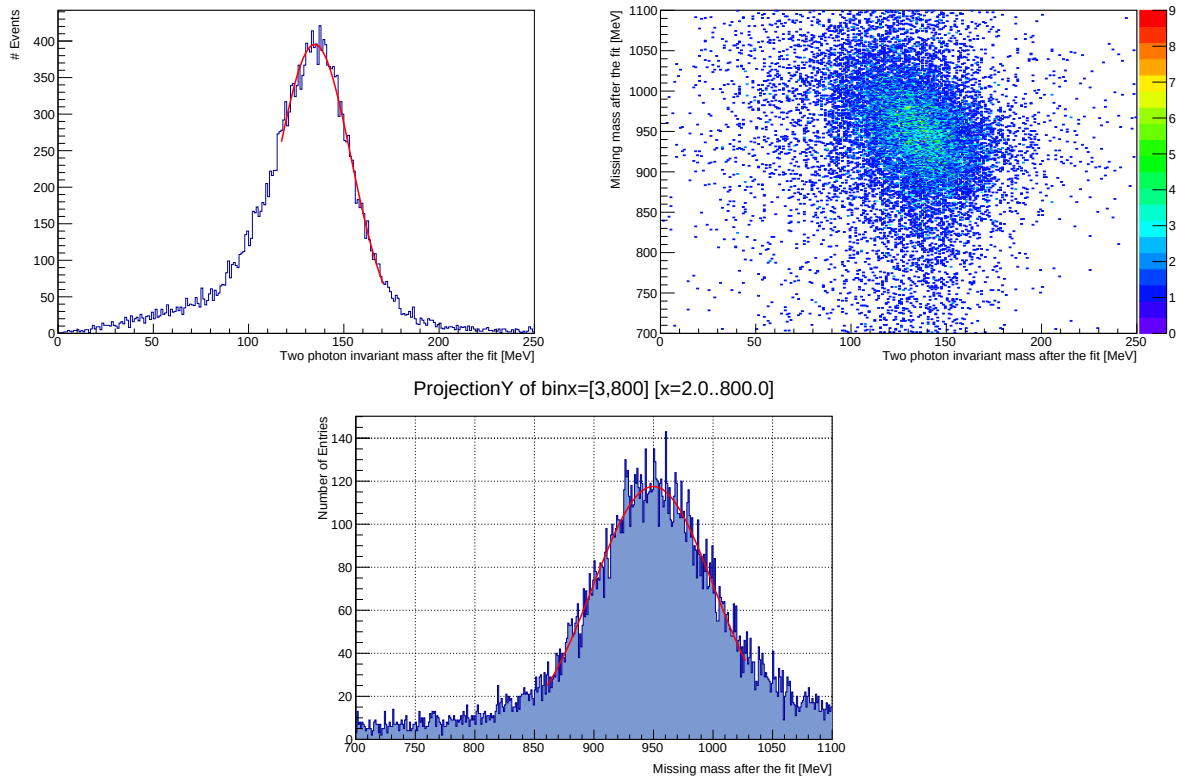

Figure 5.5.: Invariant mass distribution of the two photons (top-left), missing mass versus invariant mass of the photons (top-right) and missing mass distribution (bottom) after the fit was completed. The results of the fits are found in table 5.2

Comparing figure 5.5 to the results obtained from the standard analysis (figure 5.1) it becomes clear that the kinematic fit reduced the background drastically. Comparing the peak height in those figures, it is evident that the fit also reduced the total number of π^0s. This is also a result of the false energy calibration of the BGO, since due to that calibration issue many fits have a confidence level below the cut value of 0.015.
Fitting Gaussians to the invariant and proton mass distributions, the mean and σ of the pion and proton peak could be obtained, see table 5.2.

The results show that the kinematic fit pulled the π^0 mass close to the actual value 134.9776 MeV albeit at the expense of decreasing the accuracy of the proton mass. Furthermore the σ of both pion and proton was increased due to the fit.

Parameter	Mean [MeV]	σ [MeV]
Invariant mass	134.66 ± 0.32	19.20 ± 0.32
Proton mass	949.84 ± 0.56	50.58 ± 0.64

Table 5.2.: Mean and σ of the invariant mass distribution of two photons and the proton mass after the kinematic fit.

This simple analysis proves that the kinematic fit in general works, it selects real events and rejects false combinations of particles. Still improvements have to be done, such that the resolution of the particles is not decreased by the fit. Mainly this can be achieved by an improved energy calibration of the BGO ball, such that the two photons yield the correct π^0 mass when combined.
Furthermore the errors need to be checked again, such that χ^2 and pull-distributions look as expected from a properly working fit. Adding additional constraints (like z-momentum conservation, energy conservation, reaction vertex constraints) is another way of improvement. Since the time to establish the kinematic fitting was limited, it was not possible to work on these improvements and only the preliminary results above can be shown.
The improved fit can be applied on more complex reaction channels (e.g. $\gamma p \to \eta p \to 3\pi^0 p$) to make sure that it works with those channels. Finally the fit will be used for the already mentioned channel $\gamma p \to K^0\Sigma^+$, which was not yet observed at BGO-OD. For this fit not only momentum-conservation in all direction and energy conservation can be applied as constraints, but also the the invariant masses of the decay products of K^0 and Σ^+ as well as the reaction vertices can be constraint.

6. Summary and outlook

The goal of this work was to develop and set up an additional tagging detector and develop a kinematic fitting algorithm, both in order to increase the resolution of the BGO-OD experiment. The tagging detector (ARGUS) should improve the resolution of the initial photon energy hardware-wise, while the kinematic fit should improve the resolution of all detectors through sophisticated data analysis.
In the chapter about ARGUS this work showed, that the set goal of an increased energy resolution could be fulfilled. The ARGUS resolution is $(0.08 - 0.45)\% \cdot \mathrm{E}_0$ over an energy range of $(30 - 66)\% \cdot \mathrm{E}_0$. This is more than five times better than the current tagger energy resolution. So far only half of the detector can be read out at once, due to missing parts of the readout electronics. Once these parts have arrived ARGUS will be fully operational.
In the second part of this work a kinematic fitting algorithm was established and tested on the reaction $\gamma p \to \pi^0 p$. It could be shown that the fit works in general, although it decreases the resolution of π^0 and proton. Thus the fit still requires refinement: the energy calibrations of the involved detectors have to be checked again, additional constraints need to be applied and the errors treatment needs to be improved, in order to improve the results of the fit. The final goal is to apply the fit on the reaction $\gamma p \to K^0\Sigma^+$ to see this reaction for the first time. This goal is beyond the scope of this thesis. By then the fit will be a valuable addition to the analysis performed at the BGO-OD experiment.

A. Appendix

A.1. Figures

A.1.1. Materials

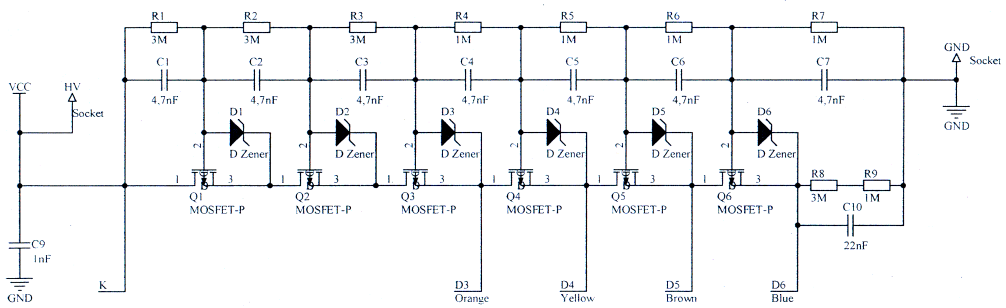

Figure A.1.: Scheme of the HV-card used to stabilise the last dynodes of the PMTs.

A.1.2. First prototype design

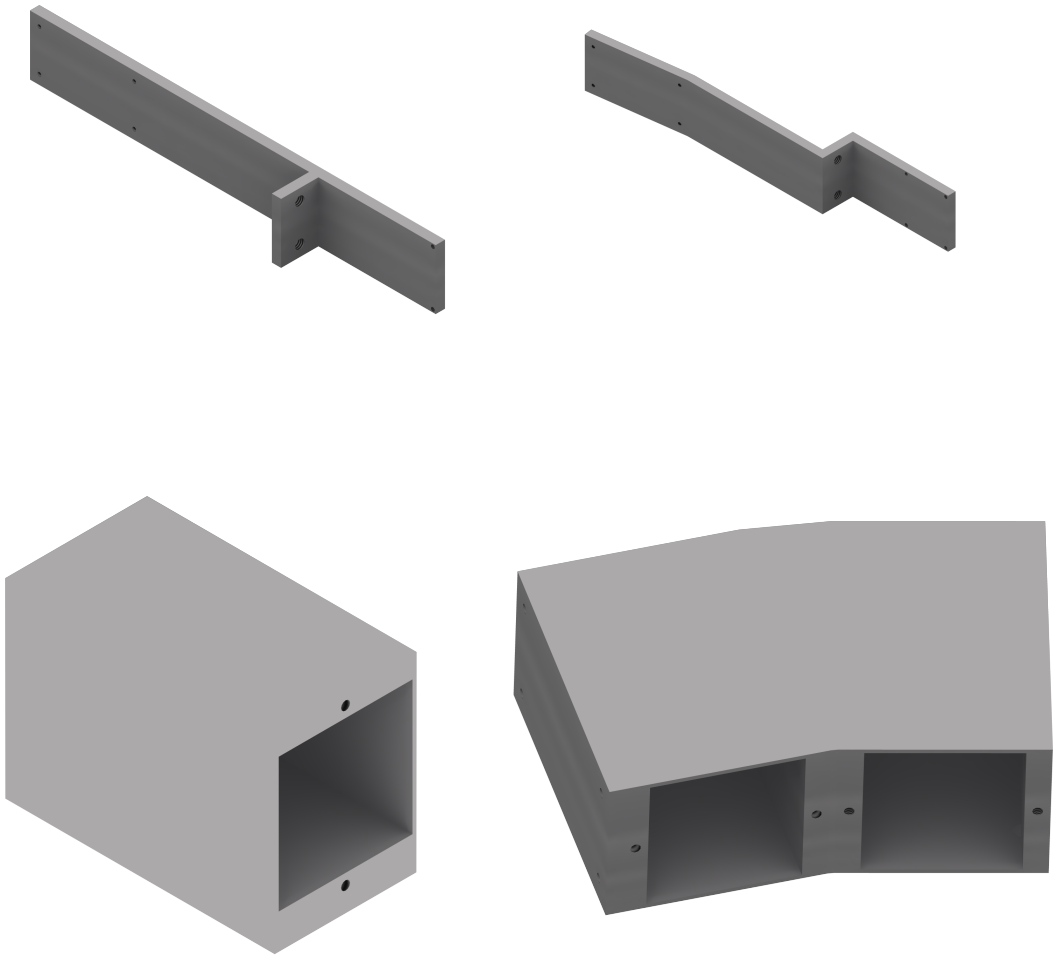

Figure A.2.: Additional pictures of the first prototype design, left to right, top to bottom: T-beam to hold the housing of the single PMT, T-beam to hold the housing for the two PMTs, housing for the single PMT, housing for the two PMTs.

A.1.3. Second prototype design

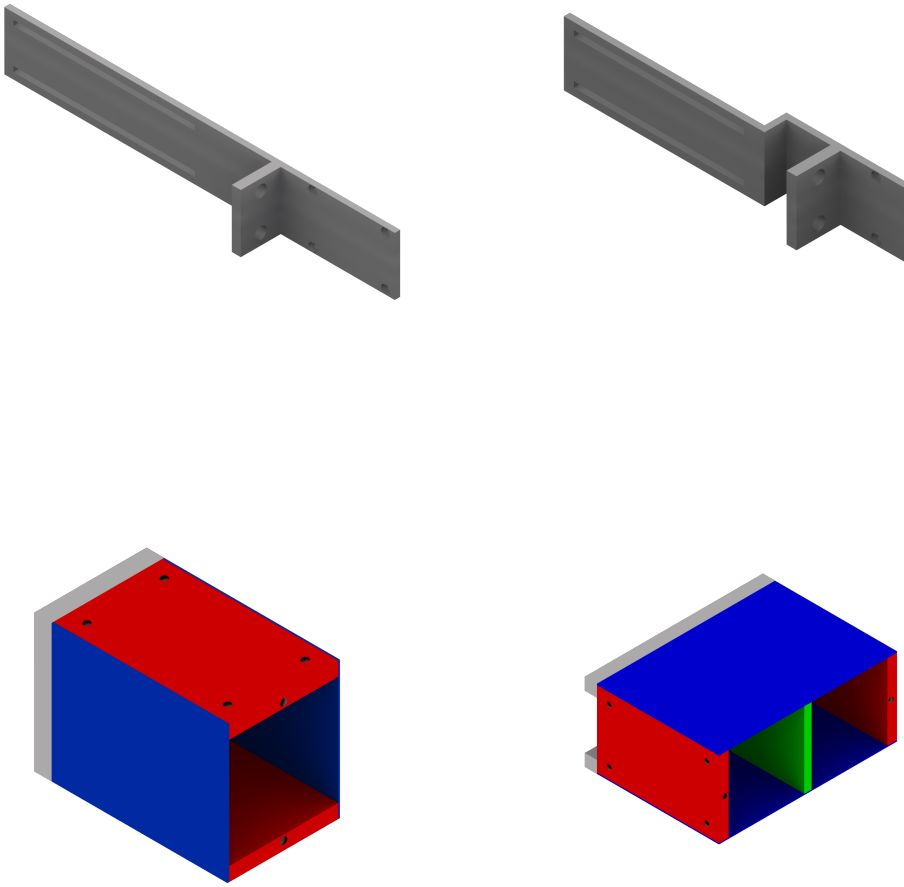

Figure A.3.: Additional pictures of the second prototype design, left to right, top to bottom: T-beam to hold the housing of the single PMT, T-beam to hold the housing for the two PMTs, housing for the single PMT, housing for the two PMTs. The different colours in the pictures of the PMT-harnesses mark the different parts of which the housings are made up to simplify the construction. The long holes in the T-beam make it possible to move the PMTs slightly if this is necessary.

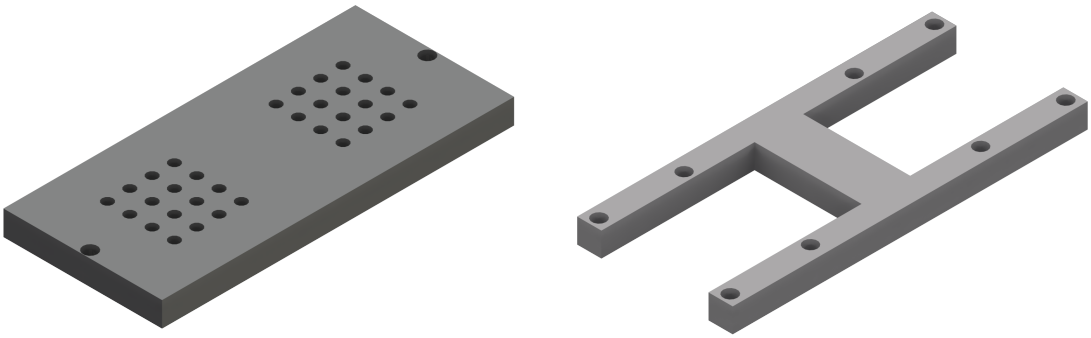

Figure A.4.: Additional pictures of the second prototype design, left to right: cap for the double-PMT-housing and end-cap for this housing.

A.1.4. Final design

Figure A.5.: Arrangement of the fibres on the double PMT side as well as the ends of the fibres in the respective PVC blocks.

A.2. Tables

PMT serial number	Anode dark current [nA]	Cathode current [$\mu A/lm$]	Anode current [A/lm]	Gain [10^6]	Voltage [V]
3803	0.28	86.4	510	5.90	750
3773	0.05	83.6	403	4.81	760
3774	5.90	82.4	465	5.64	755
3767	0.61	88.6	687	7.75	725
3747	1.10	87.1	701	8.05	725
3743	1.60	85.7	554	6.46	745
3723	0.12	80.3	574	7.15	735
3679	0.71	89.5	631	7.05	735
3553	0.45	84.5	618	7.31	735
3569	0.01	80.5	379	4.71	760
3759	0.05	85.3	826	9.68	710
3751	5.70	95.0	834	8.78	720
3754	6.20	86.4	703	8.14	725
3745	1.40	92.4	789	8.54	720
3701	1.70	87.0	418	4.80	760
3728	5.50	83.9	460	5.48	755
3715	0.02	76.3	330	4.33	785
3700	0.33	87.5	568	6.49	745
3654	0.02	88.3	353	4.00	790
3652	0.03	88.5	379	4.28	785
3627	0.03	90.1	308	3.42	800
3590	0.06	97.1	322	3.32	800
3573	0.02	93.7	347	3.70	800
3572	0.01	93.2	308	3.30	800
3401	0.05	91.8	370	4.03	790
3917	0.26	85.7	466	5.44	755
3913	0.11	91.5	736	4.77	760
3911	1.80	87.5	620	7.09	735
3854	0.14	95.7	471	4.92	760
3915	0.09	84.2	420	4.99	760

Table A.1.: Properties of the used PMTs as well as their supply voltage calculated to account for the differences in gain.

Channel	Threshold [mV]	Hysteresis[mV]	Channel	Threshold [mV]	Hysteresis[mV]
1	0.020	0.020	49	0.020	0.013
2	0.023	0.015	50	0.030	0.015
3	0.020	0.020	51	0.025	0.010
4	0.015	0.020	52	0.025	0.010
5	0.028	0.020	53	0.035	0.015
6	0.045	0.005	54	0.038	0.010
7	0.040	0.018	55	0.033	0.010
8	0.030	0.015	56	0.035	0.010
9	0.030	0.020	57	0.025	0.015
10	0.055	0.020	58	0.038	0.010
11	0.040	0.015	59	0.040	0.010
12	0.035	0.020	60	0.030	0.010
13	0.023	0.018	61	0.033	0.013
14	0.030	0.020	62	0.035	0.010
15	0.030	0.015	63	0.035	0.010
16	0.035	0.015	64	0.030	0.010
17	0.025	0.015	65	0.008	0.000
18	0.025	0.015	66	0.008	0.000
19	0.030	0.010	67	0.008	0.000
20	0.033	0.015	68	0.008	0.000
21	0.033	0.013	69	0.008	0.000
22	0.050	0.008	70	0.008	0.000
23	0.050	0.005	71	0.008	0.000
24	0.033	0.010	72	0.008	0.000
25	0.030	0.018	73	0.008	0.000
26	0.050	0.010	74	0.008	0.000
27	0.060	0.005	75	0.008	0.000
28	0.045	0.010	76	0.008	0.000
29	0.033	0.013	77	0.008	0.000
30	0.035	0.015	78	0.008	0.000
31	0.043	0.010	79	0.008	0.000
32	0.040	0.010	80	0.008	0.000
33	0.025	0.015	81	0.023	0.015
34	0.025	0.015	82	0.010	0.015
35	0.020	0.015	83	0.015	0.005
36	0.025	0.015	84	0.015	0.005
37	0.025	0.010	85	0.010	0.010
38	0.030	0.013	86	0.028	0.010
39	0.043	0.005	87	0.015	0.015
40	0.030	0.010	88	0.025	0.010
41	0.028	0.015	89	0.017	0.010
42	0.045	0.005	90	0.020	0.010
43	0.040	0.013	91	0.025	0.010
44	0.030	0.015	92	0.015	0.010
45	0.020	0.010	93	0.020	0.010
46	0.023	0.010	94	0.015	0.015
47	0.025	0.010	95	0.018	0.015
48	0.020	0.015	96	0.020	0.010

Table A.2.: Hysteresis and threshold for channel 1 to 96.

Channel	Threshold [mV]	Hysteresis[mV]	Channel	Threshold [mV]	Hysteresis[mV]
97	0.020	0.010	145	0.020	0.010
98	0.020	0.010	146	0.020	0.015
99	0.020	0.010	147	0.020	0.010
100	0.020	0.010	148	0.023	0.010
101	0.025	0.010	149	0.020	0.010
102	0.025	0.010	150	0.029	0.010
103	0.028	0.010	151	0.022	0.010
104	0.025	0.010	152	0.020	0.010
105	0.020	0.010	153	0.024	0.010
106	0.028	0.010	154	0.028	0.010
107	0.028	0.010	155	0.023	0.010
108	0.025	0.010	156	0.020	0.010
109	0.020	0.015	157	0.020	0.010
110	0.025	0.010	158	0.020	0.010
111	0.025	0.010	159	0.023	0.010
112	0.020	0.010	160	0.020	0.010
113	0.030	0.010	161	0.048	0.005
114	0.025	0.010	162	0.040	0.005
115	0.020	0.010	163	0.043	0.005
116	0.030	0.010	164	0.040	0.005
117	0.035	0.010	165	0.046	0.005
118	0.035	0.010	166	0.046	0.005
119	0.038	0.010	167	0.049	0.005
120	0.030	0.010	168	0.046	0.005
121	0.030	0.010	169	0.048	0.005
122	0.033	0.010	170	0.048	0.005
123	0.033	0.010	171	0.050	0.005
124	0.025	0.010	172	0.045	0.005
125	0.040	0.010	173	0.043	0.005
126	0.035	0.010	174	0.040	0.005
127	0.033	0.010	175	0.043	0.005
128	0.030	0.010	176	0.043	0.005
129	0.033	0.015	177	0.023	0.010
130	0.033	0.015	178	0.020	0.010
131	0.015	0.015	179	0.020	0.010
132	0.023	0.015	180	0.020	0.010
133	0.035	0.018	181	0.023	0.010
134	0.045	0.013	182	0.026	0.010
135	0.035	0.015	183	0.030	0.010
136	0.043	0.010	184	0.026	0.010
137	0.040	0.010	185	0.023	0.010
138	0.048	0.010	186	0.028	0.010
139	0.043	0.010	187	0.026	0.015
140	0.040	0.015	188	0.020	0.010
141	0.035	0.015	189	0.020	0.010
142	0.035	0.010	190	0.020	0.010
143	0.033	0.023	191	0.020	0.013
144	0.028	0.015	192	0.020	0.010

Table A.3.: Hysteresis and threshold for channel 97 to 192.

Channel	Threshold [mV]	Hysteresis[mV]	Channel	Threshold [mV]	Hysteresis[mV]
193	0.030	0.010	241	0.020	0.020
194	0.025	0.010	242	0.016	0.015
195	0.025	0.010	243	0.020	0.020
196	0.030	0.010	244	0.015	0.020
197	0.038	0.010	245	0.028	0.020
198	0.035	0.010	246	0.040	0.005
199	0.038	0.010	247	0.038	0.018
200	0.035	0.010	248	0.025	0.015
201	0.030	0.010	249	0.020	0.015
202	0.040	0.010	250	0.047	0.020
203	0.038	0.010	251	0.040	0.015
204	0.035	0.010	252	0.030	0.020
205	0.035	0.010	253	0.015	0.005
206	0.035	0.010	254	0.024	0.018
207	0.035	0.010	255	0.030	0.015
208	0.035	0.010	256	0.035	0.020
209	0.045	0.010	257	0.025	0.015
210	0.035	0.015	258	0.014	0.008
211	0.045	0.010	259	0.030	0.010
212	0.040	0.010	260	0.033	0.015
213	0.045	0.010	261	0.030	0.013
214	0.045	0.010	262	0.050	0.008
215	0.045	0.010	263	0.050	0.005
216	0.045	0.010	264	0.033	0.010
217	0.040	0.010	265	0.030	0.018
218	0.048	0.010	266	0.050	0.010
219	0.048	0.010	267	0.060	0.005
220	0.040	0.010	268	0.045	0.010
221	0.045	0.010	269	0.033	0.013
222	0.051	0.010	270	0.032	0.015
223	0.045	0.010	271	0.043	0.010
224	0.045	0.010	272	0.040	0.010
225	0.025	0.015	273	0.028	0.015
226	0.025	0.015	274	0.025	0.015
227	0.025	0.015	275	0.020	0.015
228	0.025	0.015	276	0.025	0.015
229	0.025	0.015	277	0.028	0.010
230	0.025	0.015	278	0.033	0.013
231	0.025	0.015	279	0.049	0.005
232	0.025	0.015	280	0.030	0.010
233	0.030	0.015	281	0.028	0.015
234	0.025	0.015	282	0.048	0.005
235	0.028	0.015	283	0.040	0.013
236	0.025	0.015	284	0.030	0.015
237	0.025	0.015	285	0.026	0.010
238	0.025	0.015	286	0.023	0.010
239	0.025	0.015	287	0.025	0.010
240	0.025	0.015	288	0.020	0.015

Table A.4.: Hysteresis and threshold for channel 193 to 288.

Channel	Threshold [mV]	Hysteresis[mV]	Channel	Threshold [mV]	Hysteresis[mV]
289	0.020	0.013	337	0.020	0.010
290	0.032	0.015	338	0.015	0.015
291	0.025	0.010	339	0.020	0.010
292	0.025	0.010	340	0.020	0.010
293	0.035	0.015	341	0.025	0.010
294	0.038	0.010	342	0.025	0.010
295	0.033	0.010	343	0.028	0.010
296	0.035	0.010	344	0.025	0.010
297	0.025	0.015	345	0.020	0.010
298	0.038	0.010	346	0.040	0.010
299	0.040	0.010	347	0.028	0.010
300	0.030	0.010	348	0.025	0.010
301	0.033	0.013	349	0.020	0.010
302	0.035	0.010	350	0.025	0.010
303	0.035	0.010	351	0.023	0.010
304	0.033	0.010	352	0.020	0.010
305	0.015	0.000	353	0.030	0.005
306	0.012	0.000	354	0.025	0.005
307	0.018	0.000	355	0.020	0.005
308	0.021	0.000	356	0.030	0.005
309	0.011	0.000	357	0.035	0.005
310	0.013	0.000	358	0.035	0.005
311	0.023	0.000	359	0.038	0.005
312	0.016	0.000	360	0.030	0.005
313	0.015	0.000	361	0.036	0.005
314	0.018	0.000	362	0.033	0.005
315	0.018	0.000	363	0.041	0.005
316	0.027	0.000	364	0.031	0.005
317	0.008	0.000	365	0.040	0.005
318	0.010	0.000	366	0.035	0.005
319	0.013	0.000	367	0.033	0.005
320	0.013	0.000	368	0.030	0.005
321	0.027	0.015	369	0.025	0.010
322	0.020	0.015	370	0.020	0.010
323	0.026	0.005	371	0.012	0.010
324	0.033	0.005	372	0.017	0.010
325	0.029	0.010	373	0.027	0.010
326	0.043	0.010	374	0.035	0.010
327	0.036	0.015	375	0.022	0.010
328	0.035	0.010	376	0.025	0.010
329	0.020	0.010	377	0.038	0.010
330	0.039	0.010	378	0.046	0.010
331	0.040	0.010	379	0.043	0.015
332	0.030	0.010	380	0.020	0.010
333	0.025	0.010	381	0.025	0.010
334	0.025	0.015	382	0.025	0.010
335	0.024	0.015	383	0.023	0.013
336	0.025	0.010	384	0.020	0.010

Table A.5.: Hysteresis and threshold for channel 289 to 384.

Channel	Threshold [mV]	Hysteresis[mV]	Channel	Threshold [mV]	Hysteresis[mV]
385	0.023	0.010	433	0.030	0.010
386	0.020	0.015	434	0.025	0.010
387	0.020	0.010	435	0.025	0.010
388	0.026	0.010	436	0.025	0.010
389	0.023	0.010	437	0.038	0.010
390	0.032	0.010	438	0.035	0.010
391	0.022	0.010	439	0.043	0.015
392	0.020	0.010	440	0.035	0.010
393	0.027	0.010	441	0.020	0.010
394	0.028	0.010	442	0.050	0.010
395	0.023	0.010	443	0.038	0.010
396	0.020	0.010	444	0.040	0.010
397	0.020	0.010	445	0.035	0.015
398	0.020	0.010	446	0.035	0.010
399	0.023	0.010	447	0.040	0.010
400	0.020	0.010	448	0.035	0.010
401	0.048	0.005	449	0.025	0.010
402	0.040	0.005	450	0.038	0.020
403	0.043	0.005	451	0.030	0.020
404	0.040	0.005	452	0.040	0.010
405	0.046	0.005	453	0.055	0.020
406	0.046	0.005	454	0.050	0.010
407	0.049	0.005	455	0.055	0.010
408	0.046	0.005	456	0.045	0.015
409	0.048	0.005	457	0.030	0.010
410	0.048	0.005	458	0.048	0.010
411	0.050	0.005	459	0.056	0.010
412	0.045	0.005	460	0.040	0.010
413	0.048	0.005	461	0.055	0.015
414	0.040	0.005	462	0.056	0.025
415	0.043	0.005	463	0.050	0.020
416	0.043	0.005	464	0.050	0.015
417	0.033	0.010	465	0.025	0.015
418	0.030	0.010	466	0.025	0.015
419	0.028	0.010	467	0.025	0.015
420	0.025	0.010	468	0.025	0.015
421	0.028	0.010	469	0.019	0.010
422	0.041	0.010	470	0.020	0.010
423	0.045	0.010	471	0.033	0.015
424	0.036	0.010	472	0.022	0.015
425	0.028	0.010	473	0.030	0.015
426	0.043	0.010	474	0.035	0.020
427	0.036	0.015	475	0.038	0.020
428	0.020	0.010	476	0.030	0.015
429	0.023	0.010	477	0.020	0.010
430	0.028	0.010	478	0.025	0.015
431	0.023	0.013	479	0.025	0.015
432	0.025	0.010	480	0.035	0.020

Table A.6.: Hysteresis and threshold for channel 385 to 480.

Bibliography

[1] A Theory of Strong Interaction Symmetry, in M. Gell-Mann and Y. Ne'eman (eds.) The Eightfold Way, New York, NY: W.A. Benjamin, Inc. (1964).

[2] P. Avery, Applied Fitting Theory VI: Formulas for Kinematic Fitting; June 9, 1998 [Online, accessed 31.08.2015],
http : *//www.phys.ufl.edu/* ∼ *avery/fitting/kinematic.pdf*.

[3] B. Reitz, Coherent bremsstrahlung with the scintillating fibre detector of the BGO-OD tagging system; September 2015, Master thesis, University of Bonn, in preparation.

[4] S. Glashow, Partial-symmetries of weak interactions; 1961, Nuclear Physics 22 (4): 579–588.

[5] S. Weinberg, A Model of Leptons; 1967, Physical Review Letters 19 (21): 1264–1266.

[6] A. Salam. N. Svartholm, ed. Elementary Particle Physics: Relativistic Groups and Analyticity; 1968, Eighth Nobel Symposium. Stockholm: Almquvist and Wiksell. p. 367.

[7] The 2004 Nobel Prize in Physics - Popular Information; [Online, accessed 31.08.2015],
http : *//www.nobelprize.org/nobel_prizes/physics/laureates/*2004*/popular.html*.

[8] Standard Model - Wikipedia; [Online, accessed 22.07.2015],
http : *//en.wikipedia.org/wiki/Standard_Model*.

[9] Meson - Wikipedia; [Online, accessed 31.08.2015],
https : *//en.wikipedia.org/wiki/Meson*.

[10] Baryon - Wikipedia; [Online, accessed 31.08.2015],
https : *//en.wikipedia.org/wiki/Baryon*.

[11] J. Beringer *et al.* (Particle Data Group), Review of Particle Physics; 2012, Phys. Rev. D 86, 010001.

[12] U. Löring, B. Metsch, H. Petry, The light baryon spectrum in a relativistic quark model with instanton-induced quark forces; 2001, arXiv:hep-ph/0103289v1.

[13] Crystal Barrel; [Online, accessed 31.08.2015], *http* : *//www*1*.cb.uni* − *bonn.de/*.

[14] CLAS; [Online, accessed 31.08.2015], *https* : *//www.jlab.org/Hall−B/clas−web/*.

[15] LEPS - Laser Electron Photon Experiment at SPring-8; [Online, accessed 31.08.2015], *http* : *//www.rcnp.osaka − u.ac.jp/Divisions/np*1 *− b/*.

[16] BGO-OD Experiment; [Online; accessed 23.07.2015], *https* : *//bgo − od.physik.uni − bonn.de/*.

[17] Based on: Elektronen-Stretcher-Anlage ELSA, 2015; [Online; accessed 23.07.2015], *http* : *//www − elsa.physik.uni − bonn.de/index.html*.

[18] A. Bella, Internal note.

[19] Linear, Circular and Elliptical Polarization Animation in a Single Shot - YouTube; [Online, accessed 31.08.2015], *https* : *//www.youtube.com/watch?v* = *Q*0*qrU*4*nprB*0.

[20] T. Zimmermann, Polarized Photons for the BGO-OD experiment at ELSA; NStar 2015, Osaka, 24. May - 27. May 2015.

[21] I. Brock, Feynman Graphen — Teilchenphysik — Ian C. Brock; [Online, accessed 31.08.2015], *http* : *//brock.physik.uni − bonn.de/* ∼ *brock/feynman/ktp_ws*1011*/*.

[22] Scintillation - Wikipedia; [Online, accessed 31.08.2015], *https* : *//en.wikipedia.org/wiki/Scintillation_*%28*physics*%29.

[23] Photomultiplier - Wikipedia; [Online, accessed 31.08.2015], *https* : *//en.wikipedia.org/wiki/Photomultiplier*.

[24] Saint-Gobain Ceramics & Plastics, Inc., SCG Fibres Brochure; 2005-14.

[25] H6568 (Hamamatsu) − — HTML.datasheet; [Online, accessed 31.08.2015], *http* : *//www.htmldatasheet.com/hamamatsu/h*6568*.htm*.

[26] J.I. Friedman and H.W. Kendall, Deep Inelastic Electron Scattering; December 1972, Annual Review of Nuclear Science Vol. 22: 203-254.

[27] Geant4: A toolkit for the simulation of the passage of particles through matter; [Online, accessed 01.07.2015], *http* : *//geant*4*.cern.ch/*.

[28] VMC — ROOT; [Online, accessed 01.07.2015], *https* : *//root.cern.ch/drupal/content/vmc*.

[29] LHCb collaboration, Observation of J/ψp resonances consistent with pentaquark states in $\Lambda_b^0 \to J/\psi K^- p$ decays; 2015, Phys. Rev. Lett. 115, 072001.

[30] The HERMES Collaboration: A. Airapetian *et al.*, Precise determination of the spin structure function g1 of the proton, deuteron and neutron; 2007, Phys.Rev.D75:012007.

[31] O. Freyermuth, A new FPGA-based Time-over-Threshold System for the Time-of-Flight Detectors at the BGO-OD Experiment; DPG Frühjahrstagung 2015, Heidelberg, 25. March 2015.

[32] S.-K. Choi *et al.* (Belle Collaboration), Observation of a Narrow Charmoniumlike State in Exclusive $B^{\pm} \to K^{\pm}\pi^{+}\pi^{-}J/\psi$ Decays; 23 December 2003, Phys. Rev. Lett. 91, 262001.

[33] K. Johnson, The M.I.T. bag model; 1975, Acta Physica Polonica, B6:865–892.

[34] 3D CAD Software | Inventor 3D CAD | Autodesk; [Online, accessed 05.09.2015], *http* : *//www.autodesk.com/products/inventor/overview*.

[35] B. Povh *et al.*, Teilchen und Kerne; 2004, 6. Auflage Springer-Verlag Berlin Heidelberg New York.

[36] R.H. Dalitz, T.C. Wong, and G. Rajasekaran, Model Calculation for the $Y_0^*(1405)$ Resonance State; January 1967, Phys.Rev-153, 1617.

Acknowledgment

I would like to thank Prof. Dr. Hartmut Schmieden for giving me the opportunity to work and be part of the BGO-OD experiment. I truly learned a lot and I am looking forward to continue my work at this experiment.
I also thank Prof. Dr. Philip Cole for his continuous support of our work on ARGUS and many inspiring discussions. I would like to thank Dr. Tom Jude for his help with understanding and setting up the kinematic fitting.
Thanks to all members of the work group of Prof. Schmieden and the BGO-OD collaboration, for answering my questions and generally helping me during my work.

My special thanks go to Björn-Eric Reitz for an awesome year of work together on ARGUS. It was truly a pleasure.

Last but not least I would like to thank my family and friends for their support throughout my whole course of studies.

I hereby declare that the work presented here was formulated by myself and that no sources or tools other than those cited were used.

Bonn, ...

date signature